SPACECRAFT TRAJECTORY DESIGN UTILIZING RESONANCE ORBITS IN A HYBRID OPTIMAL CONTROL FRAMEWORK

BY

DEVIN T. BUNCE

THESIS

Submitted in partial fulfillment of the requirements
for the degree of Master of Science in Aerospace Engineering
in the Graduate College of the
University of Illinois at Urbana-Champaign, 2017

Urbana, Illinois

Adviser:

Alexander R. M. Ghosh

ABSTRACT

Low-energy trajectories are a growing subset of trajectory design, particularly in the three-body space. These trajectories use the inherent stability and instability of certain orbits as a means of fuel efficient transfers. Traditionally, work on these types of trajectories has taken a very “hands on” approach from the astrodynamicist, i.e. requiring intuition and fine tweaking of parameters. This work details preliminary efforts to incorporate resonance orbits, their invariant manifolds, and associated families into an automated global optimization tool in order to create solutions of optimal impulsive spacecraft trajectories in multi-body environments. Previous work using this tool has shown the ability to use other key dynamical structures of the circular restricted three-body problem (e.g. Euler-Lagrange point orbits and their invariant manifolds) within the same automated global optimization framework to produce low-energy trajectory solutions. This work outlines necessary dynamical systems theory. Described next is how to generate resonance orbits of the first species by providing examples of the Earth-Moon and Jupiter-Europa systems. Finally shown is how these structures are used within the optimization framework. Several non-trivial impulsive trajectory problems from low-Earth to resonance orbits, resonance to resonance transfers, and resonance to Euler-Lagrange point orbit transfers are shown with Pareto front solutions.

To my family. For unyielding love and support.

ACKNOWLEDGMENTS

My accomplishments in this life are only made possible by the tremendous support and guidance from the people around me. This thesis is no exception. I need to thank my adviser, Alexander Ghosh, first and foremost. Dr. Ghosh, you have shared your knowledge and experience to advance me on this journey without holding back. Thank you for making me a part of your research group, your tremendous patience, and your friendship. You and your family have been there for me every step of the way. I am immensely grateful.

My colleagues in the Department of Aerospace Engineering were both teachers and sources of support as good friends usually are. These past two years have been an enjoyable journey because of you all. Ryne Beeson, Donald Ellison, Erik Kroeker, Vedant, Bindu Jagannatha, Marie-Caroline Corbineau, and Tristan Sarton du Jonchay, thank you for the laughs and the lessons.

This thesis would not have been possible without the continuous support of my fellow research group members Vishwa Shah and Joshua Aurich. I have no idea what would have become of me without either of you, but I am certain the best possible variant of myself exists because of the opportunities I have had to laugh and work alongside you. Thank you.

My journey at the University of Illinois would not have been possible without Dr. Victoria Coverstone. You saw something in me that other universities failed to and I am very thankful. You gave me a chance that is not given to everyone and you gave me the resources I needed to be successful. I will never forget that.

Of course, completion of this degree would not have been possible if not for my undergraduate studies at Rochester Institute of Technology and the Departments of Mechanical Engineering and Mathematics. Drs. Mario Gomes, Agamemnon Crassidis, Anurag Agarwal, Carl Lutzer, Mark Kempski, and Panchapakesan Venkataraman, you all have provided me a foundation in math and engineering. It takes a special kind of person to be a good teacher. I am fortunate that so many could be found at one institution. To my colleagues Marc Protacio, Nathan Shaw, Craig Bishop, and Lucas Sychtysz, you four have been with me since the beginning of my journey to higher education. I am grateful for the long laughs, late night study sessions, and Korean barbeque.

Brianna, our adventures began with the pursuit of our master's degrees and no amount of thanks could possibly acknowledge the pillar of support you provided. Through the challenges and victories you were by my side; thank you for everything.

In the chaotic dynamical system called life, good initial conditions are rare and for them to exist in a stable region, safe from perturbations, is even rarer still. I am fortunate to have a stable region in my family. Without my family I am sure that I would be a fraction of the man I am today. Garrett and McKaela, a brother could not ask for better siblings. You both are brimming with talent and teach me in so many special ways. I cannot wait to see the paths of success both of you create for yourselves. Mom and Dad, you two are nothing shy of a blessing and not a day has gone by that I have not been thankful for all you have been able to provide for me. You both have made sacrifices so that I might succeed and I will never forget that. I love you all more than the words on this page could ever convey.

TABLE OF CONTENTS

LIST OF TABLES

.

LIST OF FIGURES

LIST OF SYMBOLS AND ABBREVIATIONS

Δv	"Delta-V", a change in velocity
AU	Astronomical Unit
CR3BP	Circular Restricted Three-Body Problem
DyLAN	Dynamically Leveraged Automated N-body Trajectory Optimization
EMTG	Evolutionary Mission Trajectory Generation
EOM	Equation of Motion
GA	General Algorithm
GMAT	General Mission Analysis Tool
HOC	Hybrid Optimal Control
IBEX	Interstellar Boundary Explorer
MBH	Monotonic Basin Hopping
NLP	Nonlinear Programming
NSGA-II	Non-dominated Sorting Genetic Algorithm II
PCR3BP	Planar Circular Restricted Three-Body Problem
SNOPT	Sparse Nonlinear OPTimizer
STM	State Transition Matrix
3BP	Three-Body Problem
TOF	Time of Flight
TESS	Transiting Exoplanet Survey Satellite
TPBVP	Two-Point Boundary Value Problem

Chapter 1 INTRODUCTION

Spacecraft are embarking on increasingly complex missions to better understand the universe. If a mission can be successful with low amounts of fuel then the satellite gains more volume for scientific instruments. The pursuit to lower fuel requirements has spawned two main categories of mission design that are not mutually exclusive: low-thrust and low-energy mission design. Low-thrust mission design utilizes highly efficient engines, such as ion or hall thrusters, which provide much lower thrust than traditional chemical rockets. Low-thrust engines can sustain the thrust output for much longer periods of time than chemical rockets and require less fuel to do so. Low-energy mission design uses the inherent dynamics of the system to find naturally occurring trajectories to move about the system rather than onboard propulsion. Current low-energy missions are studied in a simplified Three-Body Problem (3BP), i.e. the motion of a spacecraft in the presence of two gravitational bodies. Low-energy missions use unique orbits such as resonance orbits.

A resonance orbit is a type of orbit relating two periodic trajectories. In the Three-Body Problem (3BP), these resonance orbits exist between the third body and the second body. If the third body is in resonance with the second body, then the periods are approximately related by a positive rational number which can be represented as an integer ratio. This will be explained in more detail in chapters 2 and 4.

Resonance orbits have shown significant potential for mission trajectory design. The TESS mission at NASA, to be launched later in 2017, uses a 2:1 resonance orbit in the Earth-Moon system to achieve its strict science requirements [1]. For the TESS mission, stable resonance orbits were better suited for the long duration low-energy mission when compared to other popular observation posts such as Lyapunov orbits about Euler-Lagrange points (see 2.3.2), which would have required additional station-keeping maneuvers. Resonance orbits proved to be well suited for the IBEX mission as well. IBEX is currently in a 3:1 resonance with the Moon and simulations done at NASA Goddard show stability over the next twenty years [2]. Resonance orbits are being used more frequently for their unique characteristics. It is important to build mission design tools that incorporate their dynamical structure so that they can be utilized in future mission analysis.

1.1 Background

Dynamical systems theory is a field of mathematics which focuses on understanding the behavior of complex systems by studying the dynamics, which are often modeled by differential equations. Dynamical structures are defined as groups of solutions within the dynamical system that have similar properties or characteristics. Historically, dynamical systems theory was connected to orbital mechanics when Newton began modeling the solar system using his equation for gravity in the late 1600s [3]. Euler and Lagrange made significant progress with the three-body problem by using a rotating coordinate system [4] [5]. They found areas of equilibrium, or particular solutions, to the system. Hill advanced their work further by defining infeasible solution regions [6]. Poincare defined periodicity and developed maps to determine if an orbit was periodic [7]. During this research Poincare noticed the sensitivity to initial conditions and regions of instability. Poincare maps would later become a standard technique in classifying chaotic systems [8]. This field grew and developed with several mathematicians but in the 1960s Conley began applying the techniques to find low-energy transfers to the Moon [9]. Low-energy transfers continued to be analyzed throughout the late 20^{th} century by many astrodynamicists including Howell, Lo, and Barden. Howell published several papers studying low-energy missions [10] [11] [12] and worked with Lo and Barden to design the GENESIS mission, the first flown mission to use low-energy trajectories [13]. Koon, Lo, Marsden, and Ross detailed mission design using low-energy trajectories into a staple tome of all the work done up to that point [14]. This work was complemented by a comprehensive text by Anderson and Parker [15]. Since then, use of the dynamical structures for low-energy trajectories has grown and been used on more missions such as the Solar Heliospheric Observatory (SOHO) [16] and Advanced Composition Explorer (ACE) [17], and will soon be used for the James Webb space telescope [18].

Schroer and Ott were the first to show that unstable resonance orbits could be used in low-energy trajectories by applying resonance manifolds to Earth-Moon transfers [19]. Anderson and Lo used resonance manifolds in ballistic, impulsive, and low-thrust trajectories [20] [21] [22]. They also had a series of papers which demonstrated that low-thrust transfers between resonance orbits tend to shadow the instantaneous unstable/stable manifolds of the family of resonance orbits used in transfer [23] [24] [21]. Vaquero and Howell studied resonance orbits and their manifolds on a Poincare surface of section [25]. They also showed that resonance orbits could be used for various

transfers [26] as well as connected with manifolds from Lyapunov orbits [27]. Lantoine showed that resonance manifolds could be used to find a locally optimal trajectory for moon tour transfers [28].

The above work required a human-in-the-loop approach to trajectory design. Picking patch points was often done by an astrodynamicist. For example, Vaquero's solutions relied heavily on her intuition of the dynamics when connecting Lyapunov and resonance manifolds. Recently, engineers at NASA Goddard Space Flight Center (GSFC) have developed a software tool to aid astrodynamicists in trajectory design by means of a hybrid optimal control (HOC) scheme for interplanetary missions. The Evolutionary Mission Trajectory Generator (EMTG) can generate interplanetary trajectories that are at least locally optimal in a fast and robust fashion [29].

The University of Illinois at Urbana-Champaign is developing a similar tool to that of EMTG to generate low-energy trajectories in an automated fashion by means of HOC for the three-body regime. This tool, called Dynamically Leveraged Automated N-body Trajectory Optimization (DyLAN), builds off a long history of stochastic optimization techniques applied to astrodynamics problems at UIUC [30] [31] [32] [33] [34]. The goal of the tool is to encode the intuitive methods of trajectory design that have been mentioned above to aid an astrodynamicist rather than require a human in-the-loop. DyLAN connects invariant manifolds from Lyapunov orbits (see 2.3.2), to transfer from a low Earth parking orbit to various Euler-Lagrange points in both the Earth-Moon and Sun-Earth system. Previous work on the tool has added capabilities for variable amounts of phases [35] and a grid technique to detect Poincare intersections autonomously [36] [37].

The purpose of this thesis is to add resonance orbits to the tool developed at UIUC and expand the tool's capabilities by encoding the historical intuition of resonance orbits developed over the past two decades. In doing this, the tool can use resonance dynamical structure to aid in the locally-optimal, autonomous, and rapid generation of low-energy trajectories in the three-body problem.

1.2 Thesis Overview

Chapter 2 describes the dynamical system that is used to model the trajectories throughout this thesis. Specifically, Chapter 2 begins with the n-body problem and through coordinate transformations and simplifying assumptions derives the circular restricted three-body problem.

From there, the chapter defines periodic orbits and builds a background in orbit stability and invariant manifold theory. Chapter 3 details the numeric techniques such as differential correction, multiple shooting algorithms, golden section root finding, and continuation schemes. These methods are used to generate periodic orbits and invariant manifolds in a robust fashion in the following chapters.

Building on the foundation built in Chapters 2 and 3, resonance orbits, their definition, the challenges modeling them, and behavioral characteristics such as their stability are discussed in depth in Chapter 4. The chapter focuses on generating resonance orbits in a robust and automatic way such that the orbits can be used in a hybrid optimal controller.

Chapter 5 outlines the HOC framework and software tool (DyLAN) that has been developed at the University of Illinois at Urbana-Champaign. This includes fundamental definitions of nonlinear programming (NLP), genetic algorithms, and the motivation for linking the two together. Chapter 6 combines this software tool with the techniques built in Chapter 4 to solve a few sample missions which demonstrate the capabilities of DyLAN by including resonance orbits. Chapter 7 summarizes the results of these sample missions and discusses the capabilities and limitations of this modified tool. The chapter concludes with a discussion on potential future research efforts that could expand the capabilities of DyLAN.

Chapter 2 DYNAMICAL SYSTEM

2.1 Coordinate Frames

It is often desirable to look at a particular orbit or trajectory in multiple reference frames. Each frame provides different insight to the spacecraft's motion. For the purposes of this discussion, two main coordinate frames need to be identified. Figure 2.1 shows the inertial frame in Cartesian coordinates and the circular-restricted three-body (CR3B) frame. The inertial frame is denoted by the nomenclature (X, Y, Z) and the CR3B frame is labeled as (x, y, z), with Z and z being co-axial and pointing out of the page in the positive direction.

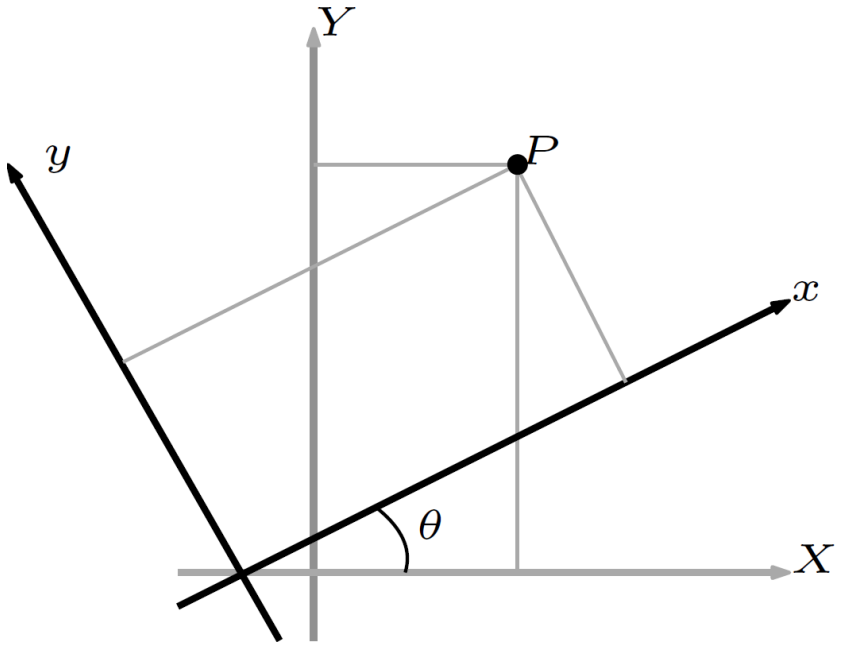

Figure 2.1 Point P with respect to both the CR3B frame and the Cartesian frame.

Section 2.1.1 details the transformation from one frame to the other. The tables of values presented later in this thesis will be in the CR3B frame.

2.1.1 Coordinate Transformation: Inertial to CR3B Frame

In the case of transforming from the inertial frame to the circular restricted three-body frame this transformation includes a rotation and a translation. The rotation is about the z-axis, which is

common between both frames, and the translation is a shift to the barycenter. The barycenter is defined as the center of mass of the system with the third body being considered massless. The translation is only in the x-direction defined as:

$$\begin{bmatrix} x_B \\ y_B \\ z_B \end{bmatrix} = \begin{bmatrix} X - \mu \\ Y \\ Z \end{bmatrix} \quad \text{Eq. 1}$$

Where μ is the ratio of the secondary mass to the total mass defined as:

$$\mu = \frac{m_s}{m_p + m_s} \quad \text{Eq. 2}$$

Where the inertial states have been nondimensionalized. Let (x_B, y_B, z_B) denote the axes in the barycenter frame. The relationship between the barycenter and rotating frames is the following:

$$\begin{bmatrix} x_B \\ y_B \\ z_B \end{bmatrix} = R_B^R \begin{bmatrix} x \\ y \\ z \end{bmatrix} \quad \text{Eq. 3}$$

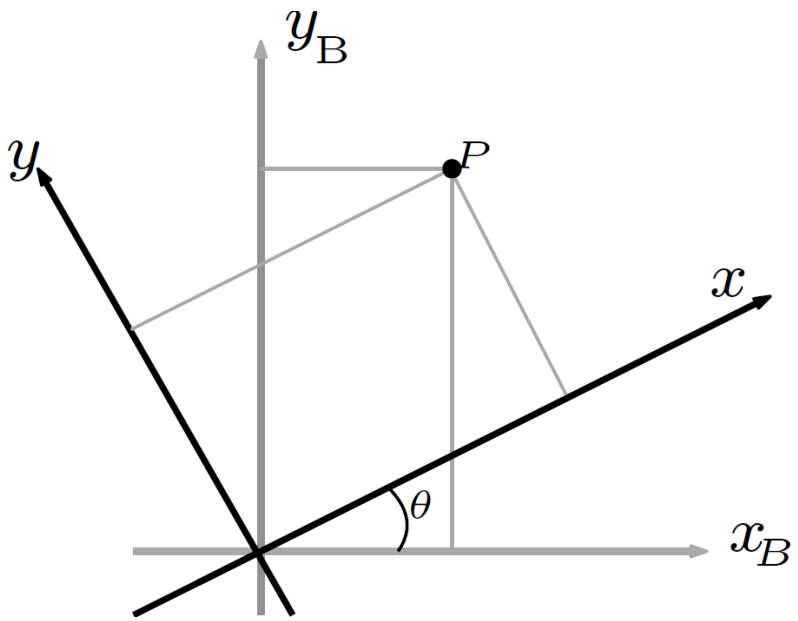

Figure 2.2 Rotating frame relative to the barycenter frame.

Where R_B^R is the rotation matrix about the z-axis. The angle between the axis grows at a constant rate because the angular velocity in the CR3B frame is constant, and in the nondimensional case

unity. Therefore, the angle between the two frames is simply $\theta = t - t_0$. With this simplification, the rotation matrix becomes the following expression:

$$R_B^R = \begin{bmatrix} \cos(t-t_0) & -sin(t-t_0) & 0 \\ sin(t-t_0) & cos(t-t_0) & 0 \\ 0 & 0 & 1 \end{bmatrix} \quad \text{Eq. 4}$$

Note, for the spatial case the rotation matrix omits the third row and third column. This rotation is insufficient to transform a state because it does not account for the velocities of the spacecraft. The transformation of a state is as follows:

$$\begin{bmatrix} x_B \\ y_B \\ z_B \\ \dot{x}_B \\ \dot{y}_B \\ \dot{z}_B \end{bmatrix} = \begin{bmatrix} R_B^R & 0_{3x3} \\ \dot{R}_B^R & R_B^R \end{bmatrix} \begin{bmatrix} x \\ y \\ z \\ \dot{x} \\ \dot{y} \\ \dot{z} \end{bmatrix} \quad \text{Eq. 5}$$

Where $\dot{R}_B^R$ is the time derivative of the rotation matrix expressed as:

$$\dot{R}_B^R = \begin{bmatrix} -\sin(t-t_0) & -cos(t-t_0) & 0 \\ cos(t-t_0) & -sin(t-t_0) & 0 \\ 0 & 0 & 0 \end{bmatrix} \quad \text{Eq. 6}$$

It is important to note that the inverse of the 6x6 state transformation matrix yields the inverse transformation.

2.2 The General *n*-Body Problem

The objective of the n-Body problem is to determine the states of all the bodies of a system as a function of time given their initial position, velocity, and masses [38] [39]. Assuming all bodies can be approximated as point masses, the equations of motion (EOM) for all the bodies can be modeled using Newtonian gravitation.

$$m_i \ddot{\boldsymbol{R}}_i = G \sum_{j=1}^{n} \frac{m_i m_j}{r_{i,j}} \boldsymbol{r}_{i,j} \qquad (j \neq i) \quad \text{Eq. 7}$$

Where $\boldsymbol{r}_{i,j}$ is the radial vector between the i^{th} and j^{th} masses. This results in $6n$ EOMs with only ten constants of integration from conservation of center of mass, angular momentum, and energy. This indicates that no analytical solution exists beyond the two-body problem (which can be solved as two one-body problems). Therefore, Eq. 7 cannot be solved in the form of an analytical solution.

However, it has been shown that lower fidelity trajectories developed in the three and four-body frame (for systems where the CR3BP assumptions are weak) hold well in the n-body simulators with only minor corrections to maintain continuity [40]. Therefore, this analysis will proceed in the three-body frame to be able to study the dynamics of the spacecraft in a more controlled fashion.

2.3 The Circular Restricted Three-Body Problem

In general, the three-body problem has the same complexity issues as the n-Body problem.

$$m_3 \frac{d^2 \boldsymbol{r}_3}{dt^2} = -G \frac{m_3 m_1}{r_{13}^3} \boldsymbol{r}_{13} - G \frac{m_3 m_2}{r_{23}^3} \boldsymbol{r}_{23} \qquad \text{Eq. 8}$$

With 18 EOMs and only ten integrals, thus Eq. 8 has no closed-form or analytic solution. The circular restricted three-body problem (CR3BP) has underlying assumptions that simplify the equations of motion to just that of the third body, in this case the spacecraft. It is assumed that the secondary body and primary body orbit around the barycenter in circular orbits, that all three masses can be approximated as point masses, and that the third body's mass is very small compared to the primary and secondary such that its motion does not alter the path of the first two. With these assumptions, the system can be translated to a rotating frame about the barycenter of the system at a constant angular velocity which is equal to the rate the first two bodies revolve around the barycenter. Figure 2.3 shows the three bodies in this frame.

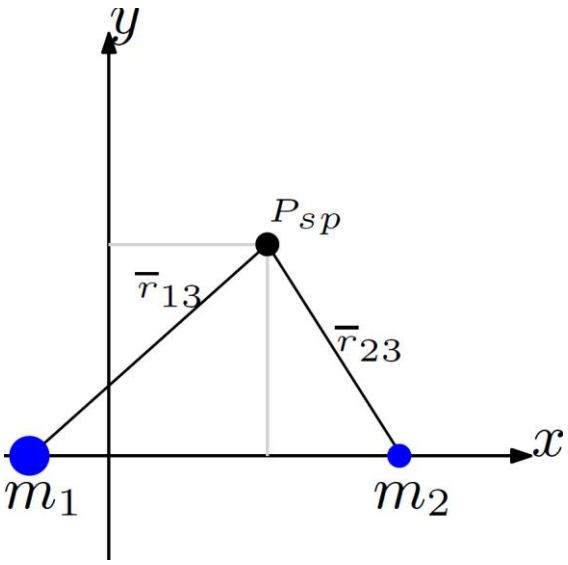

Figure 2.3 The three-body problem in the CR3B frame.

To further simplify, the system has been nondimensionalized such that the distance between the primary and secondary is unity and the period about the barycenter is 2π. Similarly, the position and velocity of the third body has been nondimensionalized by:

$$r^* = \frac{r_{dim}}{a_s}$$
$$v^* = \frac{v_{dim}}{a_s/T_s} \qquad \text{Eq. 9}$$

Where a_s is the dimensionalized semi-major axis of the secondary and T_s is the dimensionalized period of the secondary body. Thus, the positions for the primary and secondary masses are $(-\mu, 0, 0)$ and $(1-\mu, 0, 0)$ respectively.

2.3.1 Equations of Motion

Since the primary and secondary bodies remain fixed in the CR3BP framework the only equations of motion are that for the third body. To derive the EOM the relative acceleration formula of the spacecraft is used:

$$\ddot{r} = a_G + \dot{\omega}\times r + \omega\times(\omega\times r) + 2\omega\times v_{rel} + a_{rel} \qquad \text{Eq. 10}$$

Where a_G is the acceleration of the barycenter which is zero and ω is the radial velocity of the rotating frame $\omega = \sqrt{\frac{Gm_1}{r_{12}^3}}$ but is normalized to unity. Note $\hat{\imath}, \hat{\jmath}, \hat{k}$ align with the x, y, z axis in the CR3B frame.

$$\begin{aligned} r &= x\,\hat{\imath} + y\,\hat{\jmath} + z\,\hat{k} \\ \dot{r} &= \dot{x}\,\hat{\imath} + \dot{y}\,\hat{\jmath} + \dot{z}\,\hat{k} \\ \ddot{r} &= \ddot{x}\,\hat{\imath} + \ddot{y}\,\hat{\jmath} + \ddot{z}\,\hat{k} \end{aligned} \qquad \text{Eq. 11}$$

Substituting Eq. 11 into Eq. 10 and performing the mathematical operations yields:

$$\ddot{r} = (\ddot{x} - 2\omega\dot{y} - \omega^2 x)\hat{\imath} + (\ddot{y} + 2\omega\dot{x} - \omega^2 y)\hat{\jmath} + \ddot{z}\hat{k} \qquad \text{Eq. 12}$$

Summing the forces acting on the third body yields:

$$m\ddot{r} = -\frac{(1-\mu)m}{r_{12}^3}\boldsymbol{r}_{13} - \frac{\mu m}{r_{23}^3}\boldsymbol{r}_{23} \qquad \text{Eq. 13}$$

Where r_{13} and r_{23} are defined as:

$$\begin{aligned} r_{13} &= (x+\mu)\hat{\imath} + y\hat{\jmath} + z\hat{k} \\ r_{23} &= (x - 1 + mu)\hat{\imath} + y\hat{\jmath} + z\hat{k} \end{aligned} \qquad \text{Eq. 14}$$

Substituting Eq. 14 into Eq. 13 for the radial vectors, substituting unity for the radial velocity, and separating terms yields the equations of motion for the spacecraft:

$$\begin{aligned} \ddot{x} &= 2\dot{y} + x - \frac{(x+\mu)(1-\mu)}{{r_{13}}^3} - \frac{\mu(x-1+\mu)}{{r_{23}}^3} \\ \ddot{y} &= -2\dot{x} + y - \frac{(1-\mu)y}{{r_{12}}^3} - \frac{\mu y}{{r_{23}}^3} \\ \ddot{z} &= -\frac{(1-\mu)z}{{r_{13}}^3} - \frac{\mu z}{{r_{23}}^3} \end{aligned} \qquad \text{Eq. 15}$$

This is the generalized three-dimensional (or "spatial") case. The planar, or two-dimensional, circular restricted three-body problem (PCR3BP) adds an additional layer of simplification by removing motion in the z-plane while still being able to show the unique behavior of the three-body system. For numerical simplicity, the focus of this thesis will be the analysis of the PCR3BP and all the plots and state information will be represented in normalized units.

The PCR3BP is a Hamiltonian system and has an integral of motion called the Jacobi integral:

$$C(\mu, x) = -\frac{1}{2}(x^2 + y^2) + \frac{1}{2}(\dot{x}^2 + \dot{y}^2) - \frac{(1-\mu)}{r_{13}} - \frac{\mu}{r_{23}} \qquad \text{Eq. 16}$$

2.3.2 Equilibrium Points

Euler and Lagrange discovered five points in the CR3B system that are in equilibrium. They can be found by defining a potential function:

$$U = \frac{\omega^2}{2}(x^2 + y^2) + \frac{1-\mu}{r_{13}} + \frac{\mu}{r_{23}} \qquad \text{Eq. 17}$$

And solving for the case where $\frac{\partial U}{\partial x} = \frac{\partial U}{\partial y} = \frac{\partial U}{\partial z} = 0$. Essentially, these points exist where centripetal acceleration and gravitational acceleration cancel. This can be seen in detail in Prussing and Conway [39]. The result yields in three collinear points along the x-axis and two points that each make an equilateral triangle with the primary and secondary body.

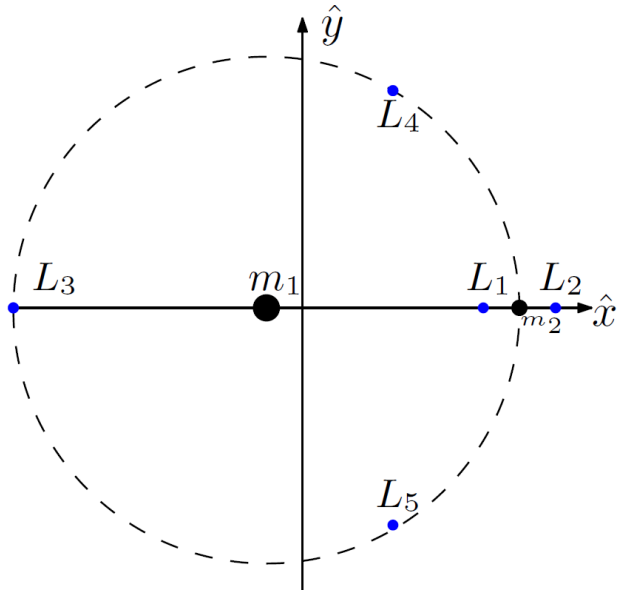

Figure 2.4 Stationary points in the circular restricted three-body problem.

These equilibrium points have been shown to have periodic orbits about them. The collinear points contain unstable periodic orbits while the equilateral points have stable periodic orbits. A periodic orbit of the PCR3BP is a trajectory such that if $\boldsymbol{x}(t_0) = \boldsymbol{x}_0$, then there exists a $T \geq 0$ such that $\boldsymbol{x}(t_0 + T) = \boldsymbol{x}_0$. The smallest such T is termed the period of the orbit. For the planar case,

these orbits are called Lyapunov orbits and for the spatial case they are called Halo orbits due to their geometry. Figure 2.5 shows example Lyapunov orbits around the L1 and L2 equilibrium points. Normalized state information for the orbits in blue can be found in Table 2.1.

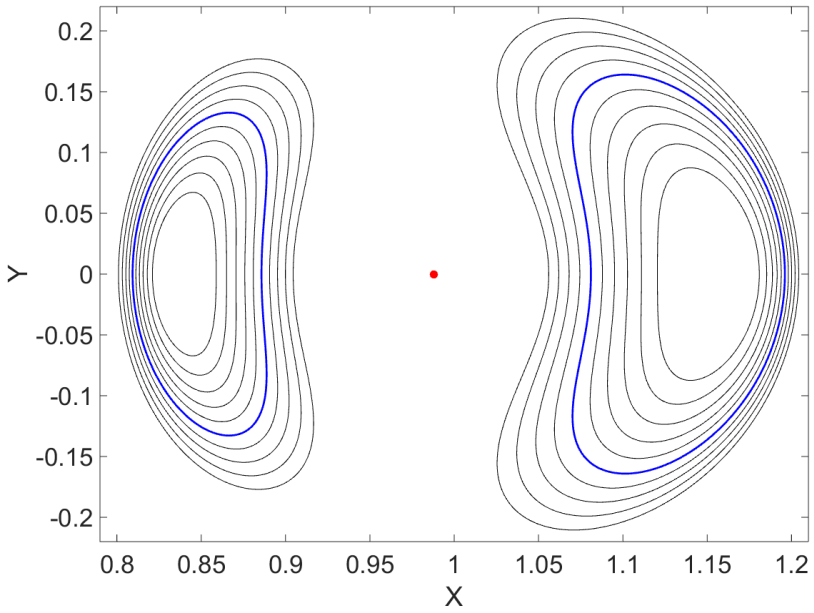

Figure 2.5 Periodic orbits of different energies around L1 and L2 in the Earth-Moon system.

Table 2.1 State information for L1 and L2 orbits.

	x	$\dot{y}$	Period (T)	Energy (C)
L1	0.8093292	0.27897327	3.0077217	-1.559192
L2	1.0810432	0.3667822	3.57440957	-1.5511045

2.3.3 Stability and Invariant Manifolds

The stability of orbits in the three-body problem is often an important design characteristic when picking an orbit for a mission. Stable periodic orbits are useful as final parking orbits in a mission because a spacecraft can spend a long mission in that orbit without much fuel for station keeping. Unstable orbits are desirable to be used as transfer trajectories from one area of space to another.

From control theory, the notion of stability can be defined from several important perspectives. This analysis uses Lyapunov stability, which analyzes the stability of equilibrium points and regions around them. Suppose there exists an n-dimensional sphere of state values about the

equilibrium point of radius ϵ and a similar sphere of radius δ where $\epsilon < \delta$. The system meets Lyapunov stability criteria if a solution $x(t_0)$ starts within ϵ of the equilibrium point then it stays within sphere $\delta\ \forall t \geq 0$. If the disturbed solution does not stay within sphere δ then the solution is considered unstable. In linear control theory, this stability can be determined from analyzing the eigenvalues and eigenvectors of the matrix A in the system of linear systems of equations $\dot{x} = Ax$. In general, the behavior of linear dynamics based on the eigenvalues and eigenvectors of the monodromy matrix can be summarized into three main groups. If all the eigenvalues have negative real components then the equilibrium point is asymptotically stable. If any of the eigenvalues have positive real components then the solution is unstable. If the eigenvalues have only imaginary components the solution is stable but not asymptotically stable.

Although periodic orbits are not a constant solution like equilibrium points, stability can be analyzed by studying the state transition matrix evaluated at one orbital period, called the monodromy matrix. For the nonlinear dynamics of the three-body problem, an approximate linear variational equations model is used. The construction and analysis of the state transition matrix is covered in more detail in Chapter 3. The stability of the periodic orbit can be determined from studying the eigenvalues of the monodromy matrix. Lyapunov's theorem states that eigenvalues from the monodromy matrix exist in reciprocal pairs. For the CR3BP a minimum pair of eigenvalues must be equal to unity. For the planar case, there are only two eigenvalue pairs. The other pair is associated with the stable and unstable space. An eigenvector associated with $|\lambda| < 1$ will approach zero as time goes to infinity and is the basis for the stable space. However, an eigenvector associated with $|\lambda| > 1$ will approach infinity as time goes to infinity and is the basis for the unstable space. Define the stability index as:

$$\nu = \frac{1}{2}(\lambda + \frac{1}{\lambda}) \qquad \text{Eq. 18}$$

Where λ and $\frac{1}{\lambda}$ are the unstable and stable eigenvalues respectively. The larger the magnitude of ν the faster the state approaches or progresses away from the periodic orbit.

The eigenvectors associated with the stable and unstable eigenvalues form a basis for the stable and unstable space respectively. Invariant manifolds are arcs to and from the periodic orbit that are formed by perturbing the state in the direction of the desired subspace. Figure 2.6 shows the four main types of manifolds that can be formed off an equilibrium point. Two stable and two

unstable manifolds can be formed by perturbing in either the positive or negative scalar multiple of the desired subspace.

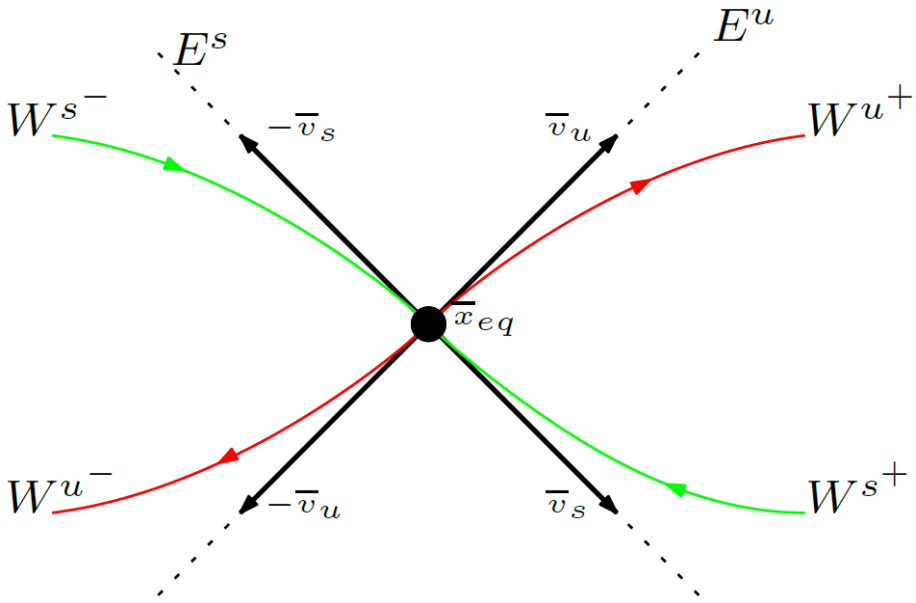

Figure 2.6 Stable (green) and unstable (red) manifolds about an equilibrium point.

Minor perturbations of the state of a spacecraft on a periodic orbit in the direction of instability cause the spacecraft to drift away from the orbit and into space when propagated *forward* in time. Similarly, perturbations in the direction of stability cause the spacecraft to drift away from the orbit and into space when propagated *backward* in time. For the planar case, these perturbations can be applied at any point along the periodic orbit in one of four directions (W^{s^-}, W^{s^+}, W^{u^-}, and W^{u^+}) which causes the spacecraft to drift to different locations in space. The manifolds are "invariant" because once on a manifold the spacecraft will stay on that manifold.

Let τ_1 be the time along the periodic orbit before the perturbation and let τ_2 be the time perturbed off an orbit. Lyapunov orbits have directions of stability and instability. The respective manifolds for L1 can be seen in Figure 2.7.

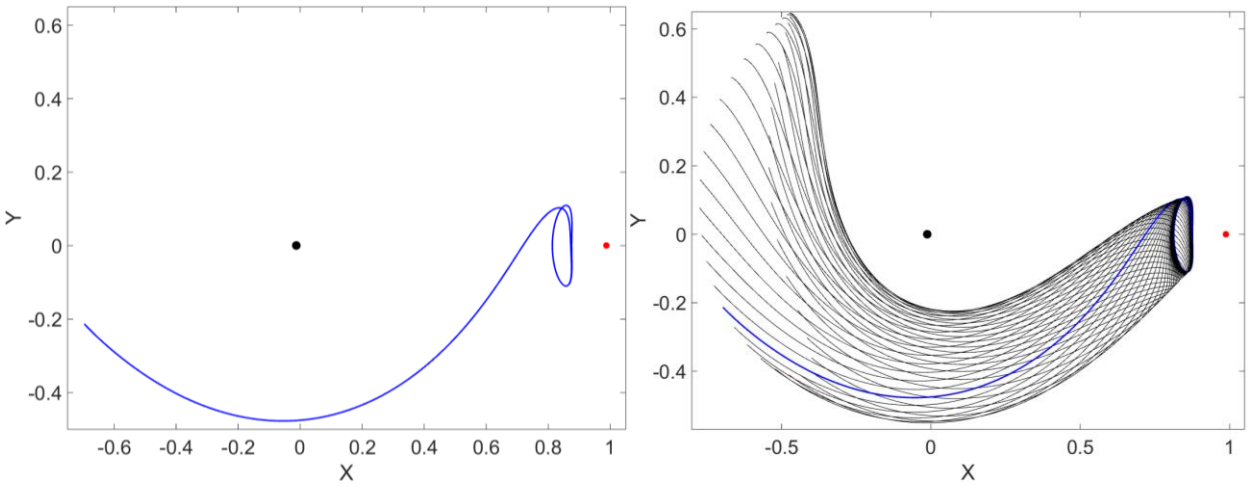

Figure 2.7 A single manifold (left) and a family of manifolds (right) in the stable direction, towards the primary body, off of an L1 Lyapunov orbit in the Earth-Moon system.

2.3.4 Poincare Surfaces

Historically, Poincare surfaces (also called "surfaces of section") have been used to connect two trajectories together [14]. This is done by selecting a plane such as the x-z plane (or some rotation of it about the barycenter) and catching states every time the trajectory intersected this plane. Figure 2.8 demonstrates determining a periodic orbit using a surface of section in a visual representation. The intersections of both trajectories are displayed on the same position vs. velocity surface. Points from both trajectories that are close together are ideal for maneuvers because only a small Δv is required to go from these two points. If the points are sufficiently close together a differential corrector can smooth out the trajectory seamlessly with no burn necessary.

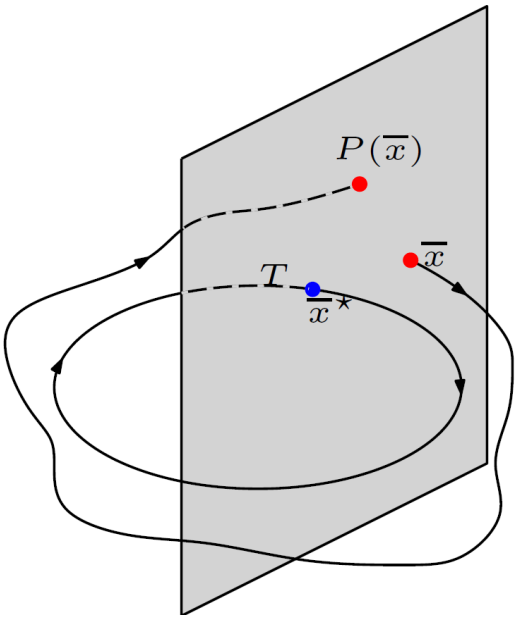

Figure 2.8 Poincare surface with a periodic solution and a non-periodic solution.

There have been recent software tools developed to detect intersections on Poincare surfaces of section in an automated fashion [36]. However, this has only been applied to Lyapunov manifolds and since resonance manifold intersections are harder to detect than Lyapunov manifolds, the tool would need significantly more development before it could be applied to this problem. Thus, this analysis does not utilize Poincare surfaces of section but automated detection and analysis would be useful additions in future work.

Chapter 3 NUMERICAL TECHNIQUES

To simulate the unique behavior of the three-body problem certain numerical tools need to be developed. These tools enable rapid generation and testing of periodic orbits so that they may be incorporated into trajectory design.

3.1 State Transition Matrix

The state transition matrix (STM) is a square matrix composed of the partial derivatives of the state.

$$\Phi(t, t_0) = \frac{\partial \boldsymbol{X}(t)}{\partial \boldsymbol{X}(t_0)} \qquad \text{Eq. 19}$$

The STM is a linearized map of the states over time. It is calculated by solving the following first order matrix differential equation:

$$\dot{\Phi}(t, t_0) = A(t, \boldsymbol{x}_t)\Phi(t, t_0) \qquad \text{Eq. 20}$$

With initial conditions $\Phi(t_0, t_0) = I_{6x6}$, for the spatial case, and $A(t, \boldsymbol{x}_t)$ is a matrix of first order partial derivatives of the equations of motion with respect to each state, that is:

$$A(t, \boldsymbol{x}_t) \equiv \frac{\partial \dot{\boldsymbol{x}}(t)}{\partial \boldsymbol{x}(t)} \qquad \text{Eq. 21}$$

Recalling the equations of motion from Chapter 2, taking derivatives of the state and calculating partials with respect to the state yields the following matrix:

$$A(t, \boldsymbol{x}_t) = \begin{bmatrix} 0 & 0 & 0 & 1 & 0 & 0 \\ 0 & 0 & 0 & 0 & 1 & 0 \\ 0 & 0 & 0 & 0 & 0 & 1 \\ \frac{\partial \ddot{x}}{\partial x} & \frac{\partial \ddot{x}}{\partial y} & \frac{\partial \ddot{x}}{\partial z} & 0 & 2 & 0 \\ \frac{\partial \ddot{y}}{\partial x} & \frac{\partial \ddot{y}}{\partial y} & \frac{\partial \ddot{y}}{\partial z} & -2 & 0 & 0 \\ \frac{\partial \ddot{z}}{\partial x} & \frac{\partial \ddot{z}}{\partial y} & \frac{\partial \ddot{z}}{\partial z} & 0 & 0 & 0 \end{bmatrix} \qquad \text{Eq. 22}$$

The partial derivatives in the lower left-hand corner are as follows:

$$\frac{\partial \ddot{x}}{\partial x} = 1 - \frac{(1-\mu)(r_1^2 - 3(x+\mu)^2)}{r_1^5} - \frac{\mu(r_2^2 - 3(x-1+\mu)^2)}{r_2^5}$$

$$\frac{\partial \ddot{y}}{\partial y} = 1 - \frac{(1-\mu)(r_1^2 - 3y^2)}{r_1^5} - \frac{\mu(r_2^2 - 3y^2)}{r_2^5}$$

$$\frac{\partial \ddot{z}}{\partial z} = -\frac{(1-\mu)(r_1^2 - 3z^2)}{r_1^5} - \frac{\mu(r_2^2 - 3z^2)}{r_2^5}$$

$$\frac{\partial \ddot{x}}{\partial y} = \frac{\partial \ddot{y}}{\partial x} = \frac{3y(1-\mu)(x+\mu)}{r_1^5} + \frac{3y\mu(x-1+\mu)}{r_2^5}$$

$$\frac{\partial \ddot{x}}{\partial z} = \frac{\partial \ddot{z}}{\partial x} = \frac{3z(1-\mu)(x+\mu)}{r_1^5} + \frac{3z\mu(x-1+\mu)}{r_2^5}$$

$$\frac{\partial \ddot{y}}{\partial z} = \frac{\partial \ddot{z}}{\partial y} = \frac{3yz(1-\mu)}{r_1^5} + \frac{3yz\mu}{r_2^5}$$

Eq. 23

The planar partials case removes rows and columns three and six from the matrix. Additionally, all z terms go to zero.

3.2 Single Shooting Differential Correction

Due to the chaotic dynamics of the three-body problem, states close to a periodic orbit may not close ($x(t_0) \neq x(t)$ for any time propagated). Initial guesses can be improved using information on the error between the initial state and final state and adjusting the initial conditions accordingly. A differential corrector is a numeric technique that uses differential information to adjust the initial state such that a periodic orbit can be found. For a more in-depth discussion on the derivation see [15]. Due to the nature of periodic orbits in the canonical frame they are symmetric about the x-axis. This means two things: solving for the whole orbit is equivalent to solving half the orbit and mirroring it, and the initial and halftime states should intersect the x-axis with only velocity in the y-direction. For the planar case, the states should be of the following form:

$$\boldsymbol{x}_0 = (x_0, 0, 0, \dot{y}_0) \quad \& \quad \boldsymbol{x}_{\frac{tf}{2}} = (x_{\frac{tf}{2}}, 0, 0, \dot{y}_{\frac{tf}{2}}) \qquad \text{Eq. 24}$$

In practice, a good initial guess will yield a state with some velocity in the x-direction at the half period, $\boldsymbol{x}_{\frac{tf}{2}} = (x, 0, \dot{x}, \dot{y})$. This state is achieved by having a conditional integrator that checks for

a $y = 0$ crossing near half the period (it may not cross exactly at half the period and therefore a time window is more appropriate). Minor adjustments of the initial conditions will adjust the final conditions but also the half period as well. To target the desired output for a given x-position the initial y-velocity is perturbed. The linearized system of equations relating the final state and the initial state is:

$$\delta \boldsymbol{x}_{\frac{tf}{2}} = \Phi\left(\frac{tf}{2}, t_0\right)\delta \boldsymbol{x}_{t_0} + \frac{\partial \boldsymbol{x}}{\partial t}\delta\left(\frac{tf}{2}\right) \qquad \text{Eq. 25}$$

Where $\delta \boldsymbol{x}_{\frac{tf}{2}}$ is the deviation in the final state due to a deviation in the initial state and orbit period. More explicitly this equation is of the form:

$$\begin{bmatrix} \delta x_{\frac{tf}{2}} \\ 0 \\ \delta \dot{x}_{\frac{tf}{2}} \\ \delta \dot{y}_{\frac{tf}{2}} \end{bmatrix} \approx \begin{bmatrix} \Phi_{11} & \Phi_{12} & \Phi_{13} & \Phi_{14} \\ \Phi_{21} & \Phi_{22} & \Phi_{23} & \Phi_{24} \\ \Phi_{31} & \Phi_{32} & \Phi_{33} & \Phi_{34} \\ \Phi_{41} & \Phi_{42} & \Phi_{43} & \Phi_{44} \end{bmatrix}\left(\frac{tf}{2}, t_0\right)\begin{bmatrix} \delta x_0 \\ 0 \\ 0 \\ \delta \dot{y}_0 \end{bmatrix} + \begin{bmatrix} \dot{x} \\ \dot{y} \\ \ddot{x} \\ \ddot{y} \end{bmatrix}\delta(\frac{tf}{2}) \qquad \text{Eq. 26}$$

The variation in the period is easiest to calculate by manipulating the second line of the system of equations in Eq. 24 such that:

$$\delta\left(\frac{tf}{2}\right) = \frac{\Phi_{21}\delta x_0 + \Phi_{24}\delta \dot{y}_0}{\ddot{y}} \qquad \text{Eq. 27}$$

Substituting this value into the third line of the system of equations yields an expression for the variation in the initial y-velocity.

$$\delta \dot{y}_0 = \frac{\delta \dot{x}_{\frac{tf}{2}} - \ddot{x}\delta\left(\frac{tf}{2}\right)}{\Phi_{34}} \qquad \text{Eq. 28}$$

Once the deviation in the initial y-velocity is calculated it is subtracted from the initial guess.

$$\dot{y}_{0,new} = \dot{y}_{0,old} - k\delta \dot{y}_0 \qquad \text{Eq. 29}$$

Where k is a dampening coefficient to control how much the y-velocity changes. If the velocity varies too much the solution can take longer to converge. Similarly, if the velocity does not vary enough it can have problems converging. Solutions in this thesis used a dampening coefficient of 0.45.

This method is iterated until $\delta \dot{x}_{\frac{tf}{2}}$ converges to zero under some desired tolerance. This method is fast for systems where the period is short and can take a couple dozen steps to converge for longer flight times. Figure 3.1 shows an exaggerated example of what the single shooting differential corrector does to an initial guess to converge upon a final solution. The solution is displayed in the rotating frame. The primary body is denoted by the black dot and the secondary body is denoted by the red dot.

Figure 3.1 Example adjustment of differential correction exaggerated.

The differential corrector converges when the states intersect the x-axis with only velocity in the y-direction at approximately half the orbital period. With half the solution generated the full orbit is generated by mirroring the states across the x-axis.

3.3 Multiple Shooting Differential Correction

Single shooting correction is limited due to its use of the STM. The STM is a linear sensitivity model. In environments where the orbit period is long the STM loses accuracy. This effect is magnified in systems with large μ coefficients because the linearized model does not capture the larger perturbations caused by the second body. The STM could maintain its accuracy if the orbit is broken into many segments and if the time of each segment is relatively short. Multiple shooting

is similar to single shooting correction except the orbit is now broken into n-segments with the desired goal being the end of each segment matching the beginning of the next segment within some set tolerance.

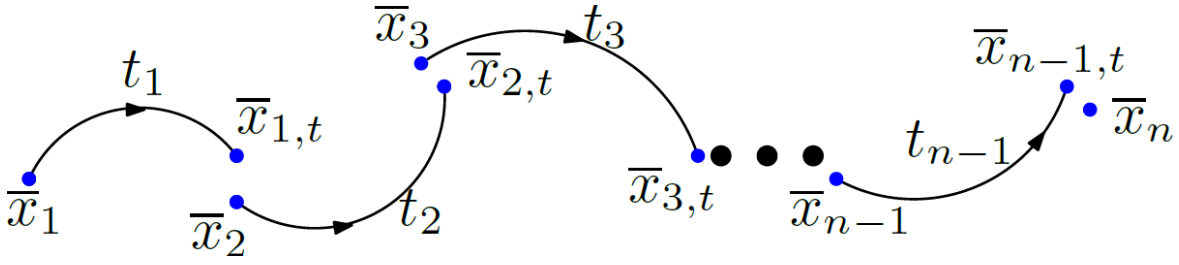

Figure 3.2 Generic multiple shooting intitial configuration.

The state vector contains the state values for each segment as well as the time of flight for the orbit:

$$X = [\bar{\boldsymbol{x}}_1, \bar{\boldsymbol{x}}_2, \dots, \bar{\boldsymbol{x}}_n, t_1, t_2, t_3, \dots, t_{n-1}] \qquad \text{Eq. 30}$$

Note that for closed orbits the sum of the time segments is the total period of the orbit. Additionally, a vector of m constraints is constructed which holds the match point constraints between each of the segments:

$$F(X) = [\bar{\boldsymbol{x}}_2 - \bar{\boldsymbol{x}}_{1,t}, \bar{\boldsymbol{x}}_3 - \bar{\boldsymbol{x}}_{2,t}, \dots, \bar{\boldsymbol{x}}_n - \bar{\boldsymbol{x}}_{n-1,t}] \qquad \text{Eq. 31}$$

Here the subscript denotes the segment the state belongs to. If the subscript includes a "t" then it is the state propagated forward in time, or the last state in the numbered arc. The constraints will vary from application to application. For example, if a full periodic orbit is being generated then an additional constraint connecting the last segment back to the first is necessary. The state vector is then updated using Newton's method:

$$X_{i+1} = X_i - k_i \cdot DF(X_i)^{-1} F(X_i) \qquad \text{Eq. 32}$$

Where i is an iteration of Newton's method and k is a scalar tuning parameter which controls the correction magnitude for each step. It has been found that stepping fully ($k = 1$) in the corrected direction can overcorrect the system and cause divergence. To avoid this, a golden section search algorithm [41] is used to control the corrected step size such that the iteration's constraint vector is minimized. This sequence will iterate until a desired convergence criteria is met such as the match point constraints meeting a certain tolerance. $DF(X)$ is the Jacobian matrix of the constraint vector defined as:

$$DF(X) = \frac{\partial F}{\partial X} = \begin{bmatrix} \frac{\partial F_1}{\partial X_1} & \frac{\partial F_2}{\partial X_1} & \cdots & \frac{\partial F_m}{\partial X_1} \\ \frac{\partial F_1}{\partial X_2} & \frac{\partial F_2}{\partial X_2} & \cdots & \frac{\partial F_m}{\partial X_2} \\ \vdots & \vdots & \ddots & \vdots \\ \frac{\partial F_1}{\partial X_n} & \frac{\partial F_2}{\partial X_n} & \cdots & \frac{\partial F_m}{\partial X_n} \end{bmatrix} \quad \text{Eq. 33}$$

For the generic case given in Eq. 30 and Eq. 31, $DF(X)$ is a sparse matrix defined as:

$$DF(X) = \begin{bmatrix} \Phi(0,\frac{t_f}{n}) & -\mathrm{I}_{6x6} & & & & \dot{\boldsymbol{x}}_{1,t} & & & \\ & \Phi(0,\frac{t_f}{n}) & -\mathrm{I}_{6x6} & & & & \dot{\boldsymbol{x}}_{2,t} & & \\ & & \ddots & \ddots & & & & \ddots & \\ & & & \Phi(0,\frac{t_f}{n}) & -\mathrm{I}_{6x6} & & & & \dot{\boldsymbol{x}}_{n,t} \end{bmatrix} \quad \text{Eq. 34}$$

Where the non-identified entries are zero. For problems defined such that $m \neq n$ the pseudo inverse is used and Newton's method takes on the following form:

$$X_{i+1} = X_i - k \cdot DF(X_i)^T [DF(X_i) \cdot DF(X_i)^T]^{-1} F(X_i) \quad \text{Eq. 35}$$

3.4 Continuation Schemes

Once a single periodic orbit is calculated, a desired parameter of that orbit can be perturbed to generate a new orbit in that orbit family. This could be a perturbation in a state parameter, energy, mass ratio μ, or a non-physical quantity along a function that is the family of solution orbits. These continuation schemes are incorporated to rapidly generate a large family of periodic orbits or generate a periodic orbit with desired characteristics.

3.4.1 Single Parameter State Continuation

Single parameter state continuation (SPSC) is a simple continuation scheme where one of the state parameters of the initial point in the orbit is perturbed and a differential correction scheme is used to close this new state. It is common to perturb the x state such that $X(t_0) = [x, y, z, \dot{x}, \dot{y}, \dot{z}]$ becomes $X(t_0) = [x + \delta x, y, z, \dot{x}, \dot{y}, \dot{z}]$. Since the new state is very similar to the previously closed state, the differential correction scheme closes in just a few iterations. This can be done several

times to get a whole family of orbits and is more likely to successfully converge with smaller perturbations. However, if the perturbation is too small the differential corrector can converge back onto the original orbit. The applications of these techniques will be discussed in detail in Chapter 4.

3.4.2 Mass Ratio Continuation

Recall the mass ratio μ is unique for given primary and secondary bodies. Therefore, to transform an orbit from one three-body system to another, the orbit could be continued along the mass ratio. For example, if a desired orbit is easily generated in the Jupiter-Europa system and a similar orbit would be useful in the Earth-Moon system, continuing along the mass ratio from one system to the other is a means of doing so. Note that an orbit which exists in one system may not exist in another, so this continuation scheme is not particularly robust but is good for preserving desirable stability characteristics between systems [42].

To continue along the mass ratio a periodic orbit must be generated for an initial mass ratio. The mass ratio is then perturbed $\mu + \delta\mu$ and the equations of motion are then updated with the new mass ratio. The differential corrector is used to close a new orbit for the new mass parameter where the previously converged orbit acts as an initial guess. This can be iterated several times until the desired mass ratio is achieved.

Chapter 4 PERIODIC SOLUTIONS

This chapter will focus primarily on resonance orbits as a dynamical structure, how to generate them, what they look like, and how they can be used for low-energy mission design.

4.1 Resonance Orbits & Families

Recall that a resonance orbit is a concept involving two periodic trajectories. In the PCR3BP, these resonance orbits exist between the third body in relation to the second body. If the third body is in resonance with the second body, then the periods are related by a positive rational number which can be represented as an integer ratio $p:q$. Here p is used to denote the number of revolutions that the third body goes around the barycenter. Similarly, q indicates the number of times the secondary body revolves around the barycenter in the same fixed amount of time.

In general, resonance orbits rarely have an exact integer relationship but can be approximated as such. Orbits of similar ratios are grouped into families and labeled as having a specific $p:q$ ratio. In the inertial frame, these orbits do not display unique geometry as they are simply highly elliptical orbits. It is the canonical frame that underlines the unique behavior of these orbits.

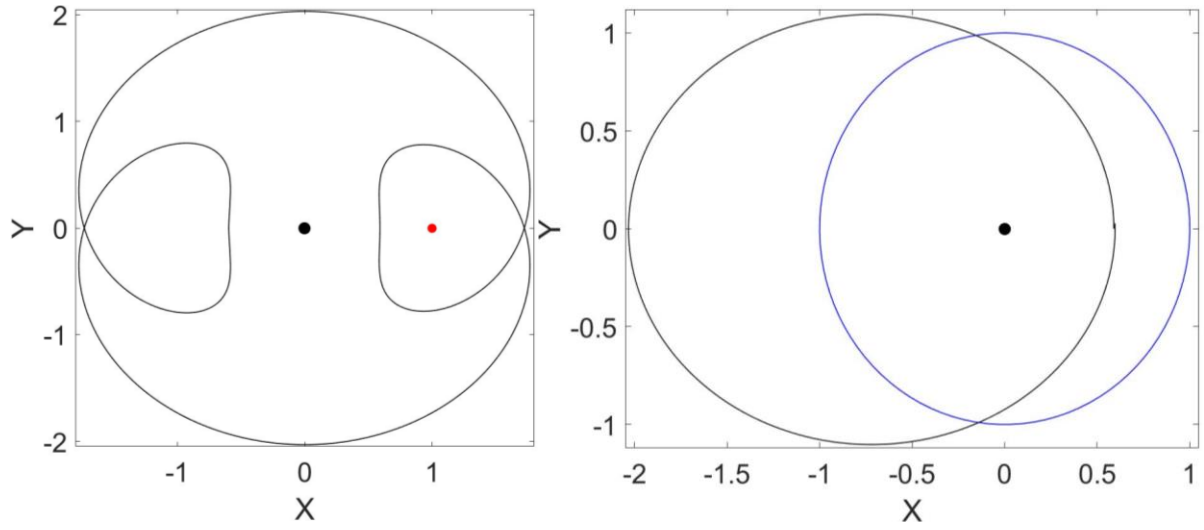

Figure 4.1 2:3 Jupiter-Europa resonance in the (a) PCR3B frame (b) inertial frame with lunar orbit with unit radius in blue.

Resonance orbits can be further subdivided into interior and exterior orbits. Interior orbits loop at apoapse in the canonical frame and are denoted by having an integer ratio greater than unity. Exterior orbits loop at periapse and are identified by having an integer ratio less than unity. Figure 4.2 gives examples of each type of orbit. The size of the loops grows with increasing eccentricity and orbits with sufficiently small eccentricity can have no loop at all.

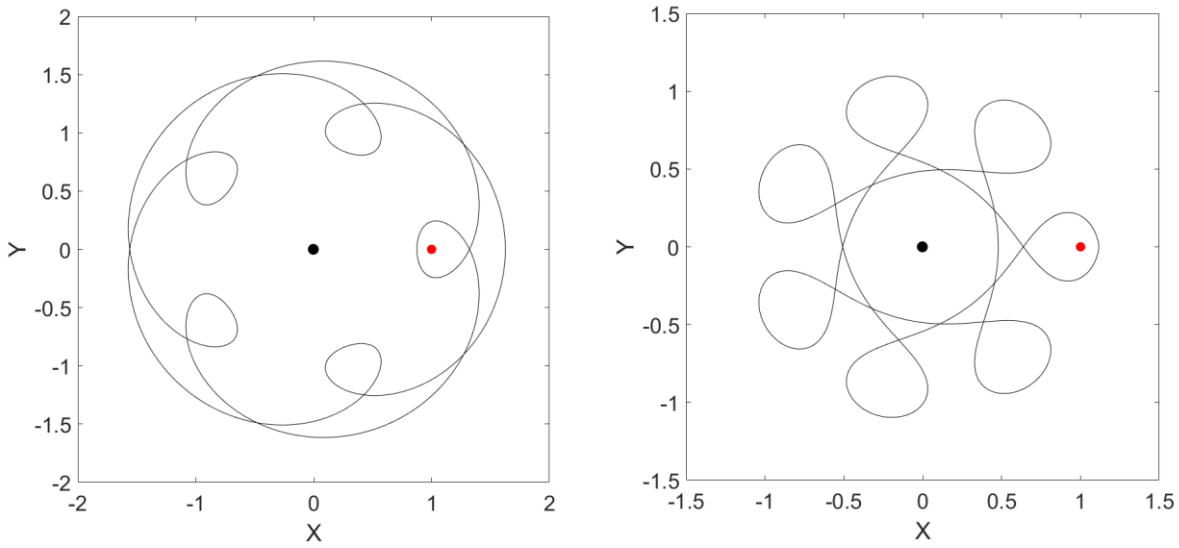

Figure 4.2 (a) A 5:7 exterior resonance orbit (b) a 7:5 interior resonance orbit; both orbits are generated in the Jupiter-Europa system.

Additionally, resonance orbits can be further subdivided into orders. If $|p-q|=1$, it is considered a first order resonance, and if $|p-q|=2$, it is a second order resonance. Higher orders can be generated and studied but this analysis will focus on first and second order resonances.

4.1.1 Two-Body Approximation

One method of generating resonance orbits is to begin with a two-body approximation and use a correction scheme to correct for any influences of the third body, in this case the addition of a moon. This approximation is very useful for three-body systems with small μ values such as the Jupiter-Europa system. Different techniques will be discussed for systems with larger μ values such as Earth-Moon. The two-body approximation is done by first selecting a desired $p:q$ ratio then calculating the semi-major axis:

$$a = \left(\mu_p T_s^2 \left(\frac{q}{p}\right)^2\right)^{\frac{1}{3}} \quad \text{Eq. 36}$$

Where μ_p is the two-body gravitational parameter of the primary body ($\mu_p = Gm_1$) and T_s is the period of the secondary, in this case the moon, about the primary. This ensures the spacecraft is in an orbit whose period will be an integer ratio of the secondary. Once the semi-major axis is calculated an eccentricity value is picked such that a desired radial value is achieved to calculate the initial x and $\dot{y}$ values:

$$r = a(1 - e) \quad \text{Eq. 37}$$

$$v = \sqrt{2\mu_p \left(\frac{1}{r} - \frac{1}{2a}\right)} \quad \text{Eq. 38}$$

The symmetry of the PCR3BP implies that resonance orbits will be symmetric about the x-axis. Therefore, the initial guess is positioned along the axis of reflection with velocity only in the y-direction. The two-body approximation must then be converted to the rotating frame, shifted to the barycenter, and converted to dimensionless units detailed in Section 2.3. A differential corrector scheme detailed in Section 3.3 can then be used to correct the initial guess so that it has the proper state vector: $\boldsymbol{x} = (x, 0, 0, \dot{y})$ at half the orbit period. This numerically derived half orbit is mirrored to show the full orbit. Iterating over various x values will generate a resonance family. If a differential corrector cannot close an orbit for a particular *x* value, then a continuation scheme is used to approach the desired orbit from previously generated orbits. This method is particularly robust for the Jupiter-Europa system due to its small μ value.

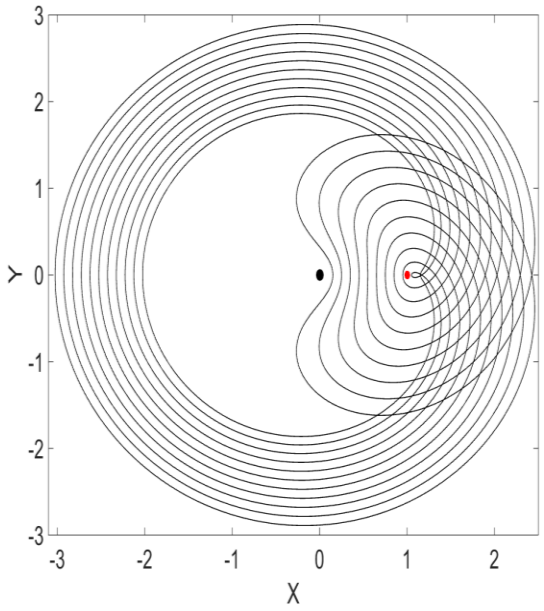

Figure 4.3 1:2 resonance family in the Jupiter-Europa system.

Using a two-body approximation with a differential corrector and continuation scheme is robust for generating families of resonance orbits which do not travel very close to the secondary body. Figure 4.4 shows a range or resonance families that can be generated with the two-body approximation and correction schemes. Figure 4.4 continued.

Table 4.1 lists normalized state information for the orbits in blue in Figure 4.4. There has been extensive analysis on resonance orbits near the secondary body [43]. This is because resonance orbits become increasingly unstable as they approach the celestial body. Resonances with close approaches have been studied as a means of slowdown flyby maneuvers when touring foreign systems such as a Europa Orbiter mission [44]. Once resonance orbits get close to the secondary they begin to dwell around the body due to its gravitational influence and the integer ratio of the periods fails. This thesis will focus on resonance orbits that are far enough from the secondary to maintain the integer ratio approximation. As a result, a significant range of Jacobi energies (Eq. 16) can still be generated which will be useful when trying to use these orbits for low-energy mission design (Chapter 5).

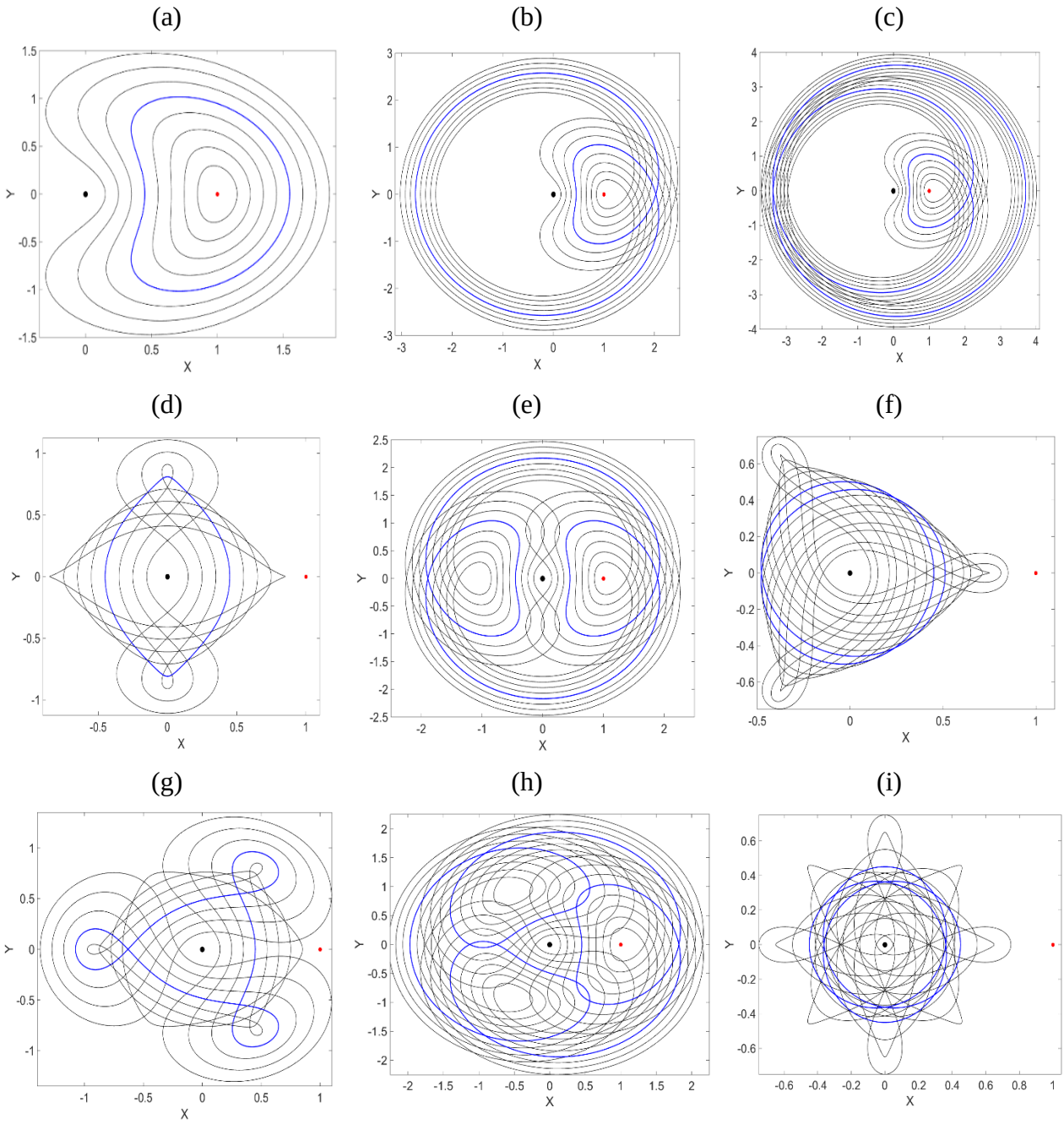

Figure 4.4 Resonance families in the Jupiter-Europa System.
(a) 1:1, (b) 1:2, (c) 1:3, (d) 2:1, (e) 2:3, (f) 3:1, (g) 3:2, (h) 3:4, (i) 4:1, (j) 4:3.

(j)

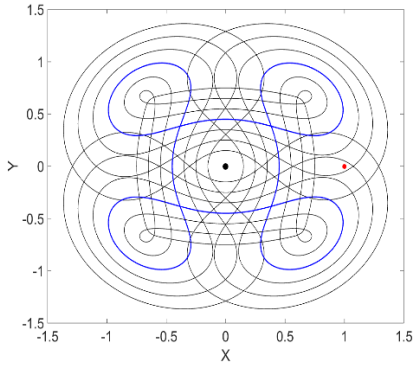

Figure 4.4 continued.

Table 4.1 Initial conditions for various resonance ratios.

Resonance Ratio	x	$\dot{y}$	Period	C
1:1	0.45	1.405837	6.28283906	-1.33514828
1:2	0.45	1.5029984	12.566055	-1.93835058
1:3	0.45	1.54083216	18.8492865	-1.13625528
2:1	0.45	1.2401521	6.282847	-1.554348579
2:3	0.45	1.4686003	18.849137	-1.244943748
3:1	0.45	1.08753667	6.2835515	-1.731969152
3:2	0.45	1.3202252	12.5662998	-1.45183985
3:4	0.45	1.45229635	25.132385	-1.268754087
4:1	0.45	0.937172633	6.28324735	-1.884190886
4:3	0.45	1.34801073	18.85033267	-1.41477069

Due to the fact that the Earth-Moon system has a higher mass ratio than Jupiter-Europa, generating resonance orbits in the Earth-Moon system is more challenging. Single shooting differential correction was insufficient at closing orbits in this system due to the larger gravitational influence of the Moon. To account for the larger mass ratio multiple shooting was used. The corrector was for the half orbit only and the initial x state was fixed so that the orbit would begin at a known location. This resulted in the state vector $X = [\dot{y}_1, \boldsymbol{x}_2, \dots, \boldsymbol{x}_n, t_1, t_2, \dots, t_n]$ and constraint vector $F = [\boldsymbol{x}_{1,t} - \boldsymbol{x}_2, \boldsymbol{x}_{2,t} - \boldsymbol{x}_3, \dots, y_{n,t} - 0, \dot{x}_{n,t} - 0]$. The initial n points were picked from a converged orbit in the Jupiter-Europa system. Since both systems are nondimensionalized, the solution points translate easily. This was done so that the initial points were already configured in a near-desired formation and as a result the differential corrector converges in a dozen or so iterations. With a strong initial guess, at least one orbit of each ratio can be generated. From there, the solution is continued in the radial direction to generate a family of orbits for a particular ratio.

Figure 4.5 shows resonance ratios in the Earth-Moon system using this technique. Figure 4.5 continued.

Table 4.2 provides normalized state information for the orbits in blue.

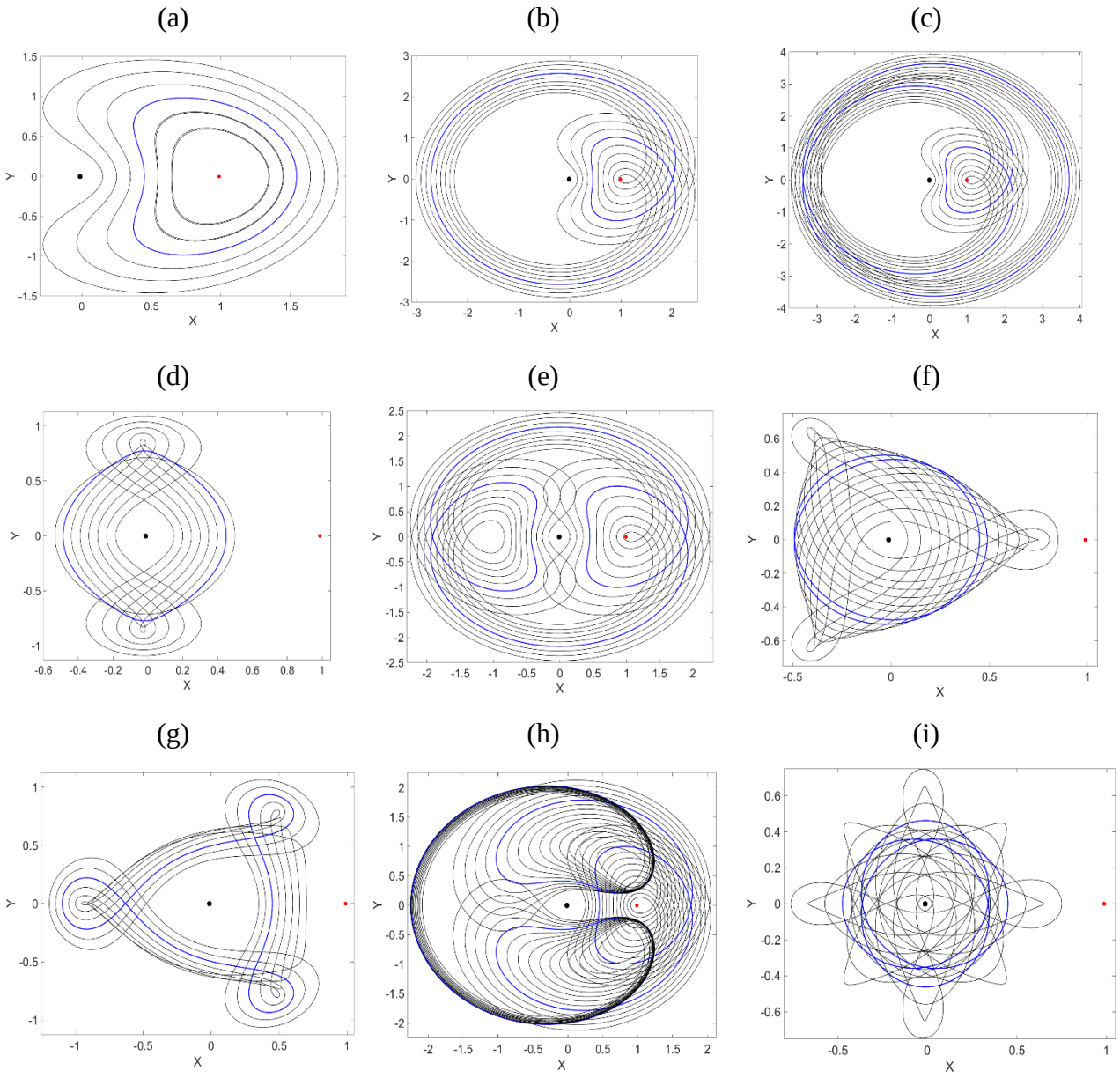

Figure 4.5 Resonance families in the Earth-Moon system.
(a) 1:1; (b) 1:2; (c) 1:3; (d) 2:1; (e) 2:3; (f) 3:1; (g) 3:2; (h) 3:4; (i) 4:1; (j) 4:3.

(j)

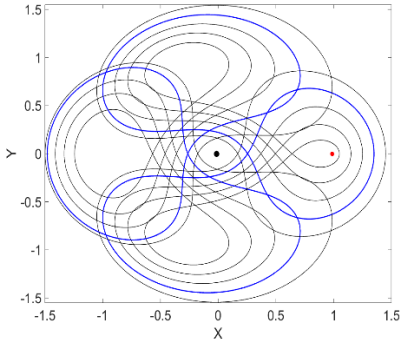

Figure 4.5 continued.

Table 4.2 Initial conditions for various resonance ratios.

Resonance Ratio	x	$\dot{y}$	Period	C
1:1	0.45	1.36819893	6.07127552	-1.32534735
1:2	0.45	1.47163198	12.391121	-1.178481163
1:3	0.45	1.5108353	18.687292	-1.120019889
2:1	0.45	1.179861504	6.0907361	-1.56529492
2:3	0.45	1.4362871149	18.635858	-1.229236809
3:1	0.45	1.036747	6.4671316	-1.723909116
3:2	0.45	1.26986973	12.499695	-1.45504694
3:4	0.45	1.4086672	25.5351434	-1.2691598
4:1	0.45	0.877146223	6.319133	-1.876638756
4:3	1.35	-0.9536793	18.7068434	-1.215266474

4.2 Periodic Stability and Manifolds

Once a desired resonance orbit is generated, it is useful to investigate the stability of the orbit. Stability analysis can be achieved using Floquet theory [45] which was detailed for periodic orbits about the Euler-Lagrange points in Section 2.3.3.

Stable resonance orbits are of interest due to their ability to serve as long term parking orbits for science missions with little to no station keeping required. Unstable orbits are also of interest since it implies the existence of both stable and unstable invariant manifolds which provide means of low-energy transport within the three-body system. This is analogous to invariant manifolds of

Lyapunov and Halo orbits about the unstable Euler-Lagrange points. Figure 4.6 shows a stable manifold off a 2:3 resonance orbit in the Earth-Moon system. This orbit is stable and therefore takes a couple revolutions about the periodic orbit before drifting into space. The perturbation magnitude is small so that the system would asymptotically approach the periodic orbit. The perturbation magnitude for this work is 1E-6.

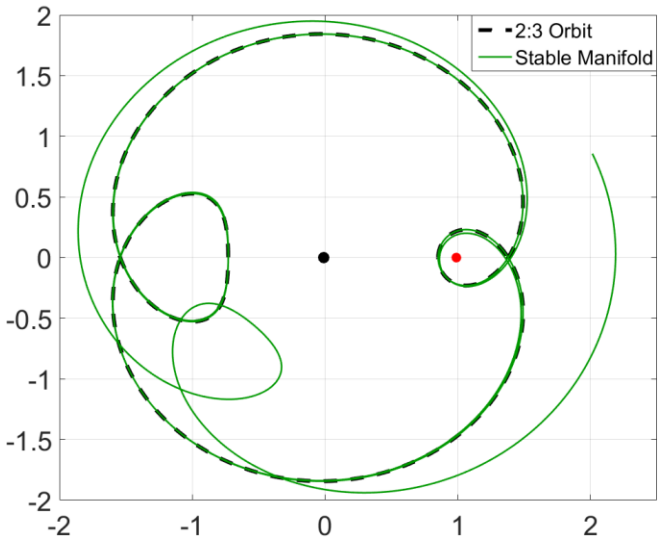

Figure 4.6 Earth-Moon 2:3 resonance with a stable manifold arc corresponding to $\tau_1 = 10.3\ (\approx 0.6\,T)$ and $\tau_2 = 60$.

Figure 4.7 shows several manifolds off a 1:2 resonance orbit. The green arcs indicate stable manifolds which approach the periodic orbit when integrated forward in time. The red arcs are unstable manifolds which flow away from the periodic orbit when integrated forward in time. The motion of the manifolds is not as uniform as it was for the Lyapunov orbits in Figure 2.7 (b). With the generation of a range of resonance orbits and their manifolds, this dynamical structure can be used for low-energy trajectory design.

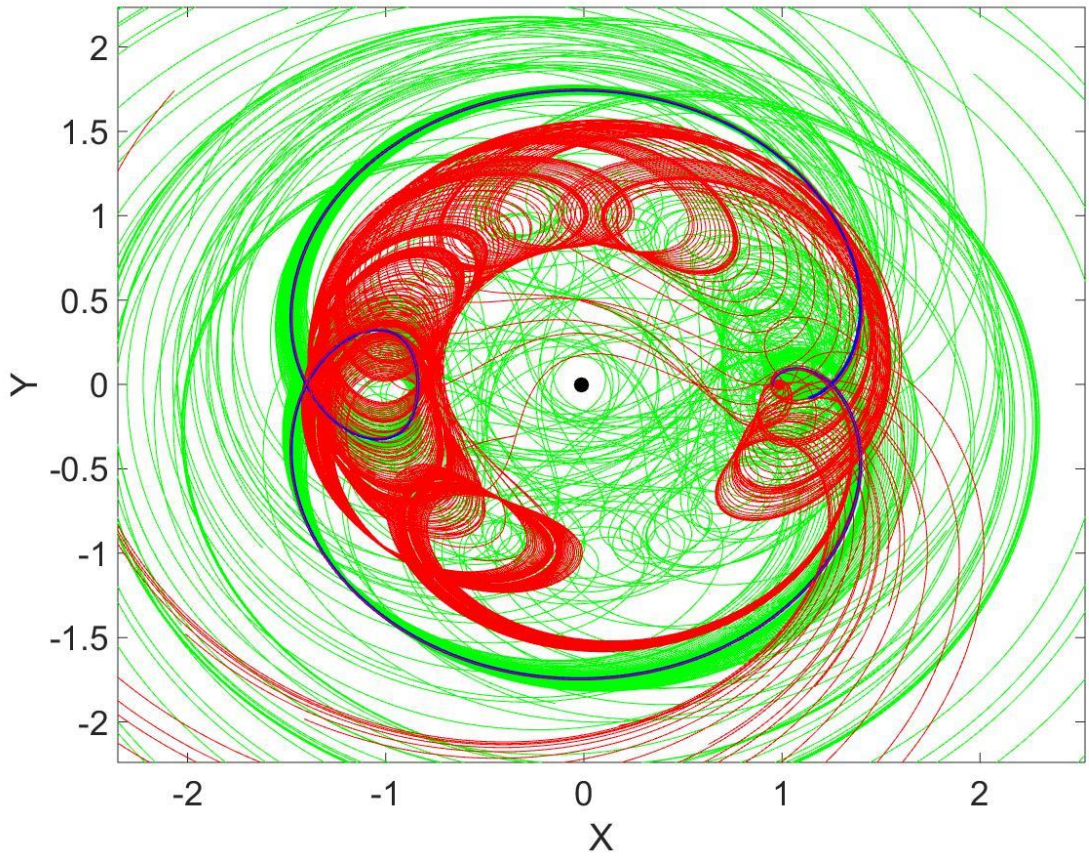

Figure 4.7 Earth-Moon 1:2 resonance orbit with stabile and unstable manifolds at 40 even τ_1 intervals for τ_2 of 60.

Chapter 5 TRAJECTORY DESIGN & OPTIMIZATION

Trajectory design is a challenging endeavor that usually requires multiple iterations to converge upon a solution. There are several different techniques and methods for designing a trajectory from one point to another. Historically, trajectory design has relied heavily on the intuition of an astrodynamicist whose years of experience and understanding of the dynamical system are used to piece together a feasible trajectory that meets the spacecraft's constraints. For example, there has been some preliminary work showing that resonance orbits as well as their manifolds can be used for low-energy transfers within the three-body framework [26]. That analysis was successful but required multiple lengthy steps to generate a trajectory. The steps included identifying key periodic orbits that would be used for the trajectory, propagating their respective manifolds, plotting the intersecting manifolds on a surface of section, picking a point within the areas of intersection that connects the two manifolds, and differentially correcting the trajectory to smooth out any discontinuities. This process is iterated over a range of orbit energies until a feasible solution is found. The problem space grows with each additional phase of the trajectory and takes a lot of theoretical understanding to know how to tweak the parameters properly. Additionally, initial conditions and constraints of the spacecraft are capricious and any significant changes could require a whole new trajectory. As a result, preliminary trajectory design that relies heavily on a human in-the-loop can be computationally and financially expensive.

Since the late 1950s, optimal control techniques have been used for trajectory design [46]. The motivation for these techniques was to derive trajectories from financially driven constraints such as minimizing fuel (Δv) or minimizing time of flight (TOF). However, due to the chaotic nature of the dynamical systems, these solutions are only locally minimum, and it is difficult to prove if a solution is a true global minimum. Therefore, deriving solutions relies on nonlinear programming techniques (see Section 5.1.2).

Due to the sensitivity to initial conditions, optimal solvers have been paired with an outer loop which performs an educated search over bounded initial conditions. These outer loops often use evolutionary algorithms such as particle swarm algorithms or genetic algorithms. Recently, astrodynamicists at NASA GSFC have had success with such a hybrid optimal controller (HOC) for interplanetary trajectory design [47]. This success has motivated the University of Illinois to

develop a similar tool (DyLAN) for trajectories in the three-body problem as a means of automating the design process and transferring the computational and iterative burden from the designer to the computer [35].

5.1 Trajectory Design

For the purposes of this thesis, a mission is defined as going from an initial parking orbit to a desired final parking orbit. A phase is defined as going from one parking orbit to another. Figure 5.1 provides a cartoon representation of the distinction between a mission and a phase.

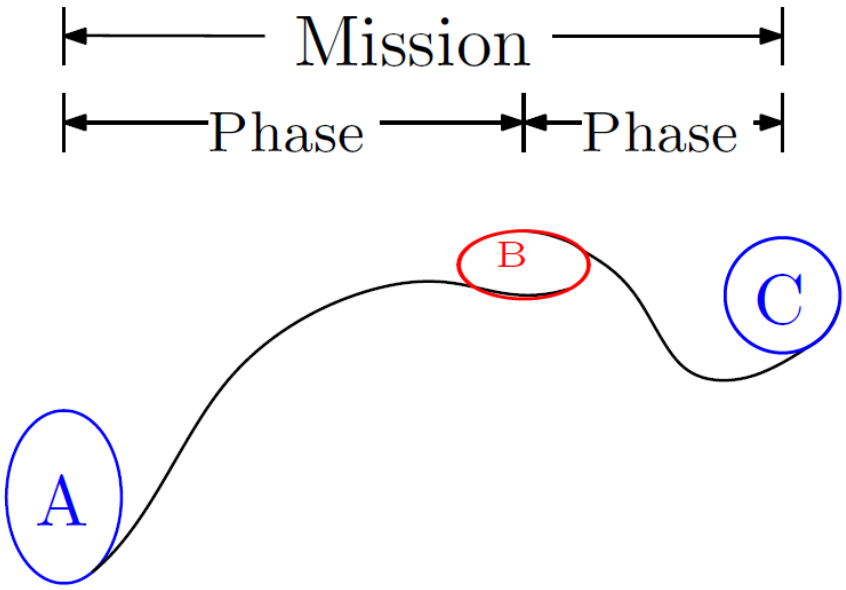

Figure 5.1 Demonstration of two-phase mission. A and C are initial and final parking orbits. B is an intermediate parking orbit.

Therefore, a "single-phase" mission is one where the trajectory goes directly from the initial parking orbit to the final parking orbit. An example of a single-phase mission is going from LEO to a parking orbit about the L1 Euler-Lagrange point. A "two-phase" mission includes an intermediate parking orbit between the initial orbit and final orbit for a nontrivial period of time. An example of a two-phase mission is to go from LEO to a parking orbit about the L1 Euler-Lagrange point to a final parking orbit about the Moon. Missions with multiple phases have multiple intermediate parking orbits.

The purpose of breaking up a mission into phases is to isolate the dynamical systems used to find low-energy trajectories for each phase. For example, the two-phase mission to the Moon can utilize stable manifolds onto a periodic orbit about the Euler-Lagrange L1 point for the first phase and then an unstable manifold off the periodic orbit towards the Moon for the second phase. There are multiple decision variables that need to be determined to find a low-energy trajectory with desirable characteristics. These variables include the time along the initial parking orbit before performing a burn, the time coasting before the spacecraft injects onto a manifold, the time along the manifold (recall this was labeled τ_2 in Section 2.3.3), and the time along the periodic orbit associated with the manifold (recall this was similarly labeled τ_1). The number of time variables grows with each additional phase. There are also Δv decision variables that are the magnitude and direction of the change in velocity each time a burn is performed. Lastly, there are energy decision variables which determine the Jacobi energy of the dynamical structure such as a periodic orbit about an Euler-Lagrange point. The Jacobi energy of that dynamical structure will determine its shape and therefore the reachability space of its invariant manifolds.

A low-energy trajectory has desirable characteristics if it minimizes financial or logistical cost functions. Two common costs are fuel and time of flight. For chemical impulse thrusters, those costs take the following form:

$$\Delta v = \sum_{i=1}^{n} \sqrt{\Delta v_{i,x}^2 + \Delta v_{i,y}^2} \qquad \text{Eq. 39}$$

$$TOF = T_{parking} + T_{transfer} + T_{manifold} \qquad \text{Eq. 40}$$

Where $T_{parking}$ is the time along the initial parking orbit, $T_{transfer}$ is the time from the parking orbit to an invariant manifold, and $T_{manifold}$ is the time along both the invariant manifold and periodic orbit it is attributed to ($\tau_1 + \tau_2$). Similarly, the Δv cost function is the sum of the resultant changes in velocity at each impulse. These two cost functions often conflict with each other, such as minimizing one often results in increasing the other. Therefore, for preliminary mission design, it is often desirable to generate a trade space of solutions so that the astrodynamicist can pick the ideal tradeoff based on the needs for a specific mission.

It is clear a mission can involve a large design space which is often difficult to navigate in order to find a trajectory which locally minimizes the cost functions. DyLAN solves missions using a

two-loop approach. The purpose of the outer loop is to evaluate the cost functions and adjust phase-level decision variables, i.e. the parking orbit variables and the dynamical structure variables such as energy, τ_1, and τ_2. The purpose of the inner loop is to find Δv's which minimize the two-point boundary value problem (TPBVP) between the parking orbit and the invariant manifold arc.

5.1.1 Outer Loop

As mentioned, the purpose of the outer loop is to choose phase level continuous and discrete decision variables that optimize the mission. For multi-objective problems (problems with multiple cost functions), this can be done two ways: using a single function and an appropriate weighting scheme:

$$\begin{cases} Minimize\ F(\bar{x}) = \sum w_i f_i(\bar{x}) \ \text{ subject to:} \\ \bar{x}_{lb} \leq \bar{x} \leq \bar{x}_{ub} \\ A\bar{x} = 0 \\ c(\bar{x}) \leq 0 \end{cases} \quad \text{Eq. 41}$$

Where w_i are scalar weights for each cost function, $\bar{x}_{lb}$ and $\bar{x}_{ub}$ are lower and upper bounds on the state values, $A\bar{x}$ is a system of linear equality constraints and $c(\bar{x})$ is a vector of nonlinear constraints. Multi-objective problems can also be solved by keeping the objectives separate:

$$\begin{cases} Minimize\ \bar{J}(\bar{x}) = [J_1(\bar{x}) \quad J_2(\bar{x}) \quad \dots \quad J_n(\bar{x})]^T \text{ subject to:} \\ \bar{x}_{lb} \leq \bar{x} \leq \bar{x}_{ub} \\ A\bar{x} = 0 \\ c(\bar{x}) \leq 0 \end{cases} \quad \text{Eq. 42}$$

Minimizing Eq. 42 results in a trade space of solutions. This trade space is often called a "Pareto front" [48]. A Pareto front is a solution set where each member in the space is better than all its neighboring solutions in at least one objective. For a two-dimensional optimal control problem, a converged family of solutions would produce a solution set similar to what is seen in Figure 5.2.

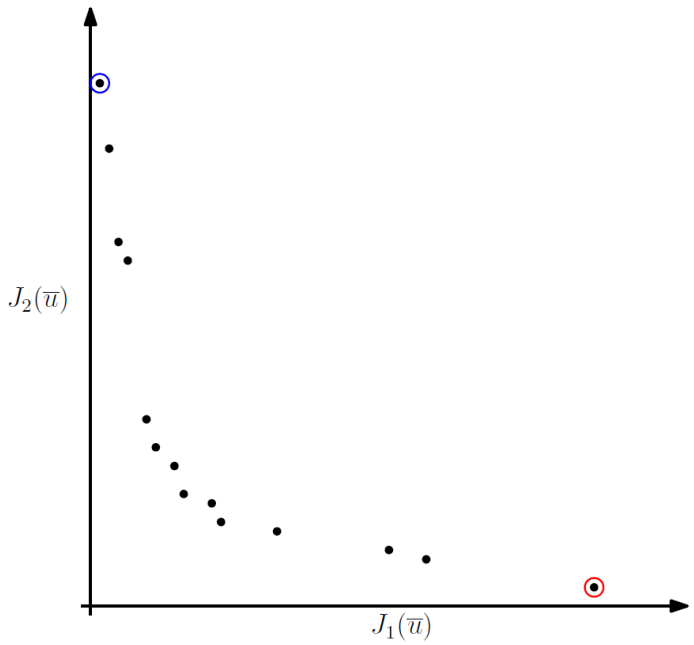

Figure 5.2 Sample Pareto front for two objective case. Single objective minimal $J_1(\bar{x})$ in blue and single objective $J_2(\bar{x})$ in red.

There are multiple techniques for the outer loop process, each with their own capabilities and limitations. For DyLAN, a genetic algorithm (GA) is used due to its ability to scale well with multiple constraints and its recent success in interplanetary trajectory design applications [47] [49].

5.1.1.1 Genetic Algorithm

A genetic algorithm replicates the natural selection process by controlling a population of solutions and evolving them towards a converged solution set. For the multiple objective case, the population evolves towards a Pareto front solution space. In this application, each individual in the population has a unique combination of decision variables that define a trajectory. During the initialization of this algorithm the phase decision variables are picked at random from a design space bounded by the user. Each individual has a TPBVP which is then locally optimized using nonlinear programming techniques (see Section 5.1.2). Once locally optimized, the individuals are then evaluated on how well they meet the cost functions. Once the individuals have been ranked they are paired at random and "mate" to create two new children that have combinations of phase v from their parents. Mutations can occur during the reproduction process to further randomize the design space and diversify the population. The children are then locally optimized and ranked as

well. Once both generations are ranked, the half of the population who has the worst rank is thrown out. This process repeats until a desired number of generations is satisfied. If the solution set does not form a Pareto front, i.e. the points in the set are not better in at least one $J_i(\bar{x})$ than their nearest neighbors, then the process is repeated with a higher generation cap. If that solution does not converge to a Pareto front then the HOC is unable to find feasible solutions and the bounds of the states need to be adjusted. For the examples studied here, the outer loop is minimizing two objectives: time of flight (TOF) and Δv. This means an individual that has a low TOF and low Δv will rank highly and have future generations derived from it. Shah's work provides a thorough exploration and discussion of this framework [50].

5.1.2 Inner Loop: Local Optimization

Recall the purpose of the inner loop is to solve the two-point boundary value problem from the initial parking orbit to the final desired parking orbit for a particular phase. For trajectories that result in multiple dynamical systems, multiple TPBVPs are solved sequentially. Often, TPBVPs are solved by breaking the trajectory into two parts, a forward arc and a backward arc, and minimizing the differences at the match point for both position and velocity such that the solution is continuous. Nonlinear programming is the process to solve an optimization problem which can be put in the form of Eq. 43:

$$\begin{cases} Minimize\ f(\bar{x})\ \text{subject to:} \\ \bar{x}_{lb} \leq \bar{x} \leq \bar{x}_{ub} \\ A\bar{x} = 0 \\ c(\bar{x}) \leq 0 \end{cases} \qquad \text{Eq. 43}$$

Due to the nature of astrodynamics problems the Jacobian matrix of the NLP tends to be sparse. Therefore, the solver used is the Sparse Nonlinear OPTimizer (SNOPT) [51] which uses gradient information to converge upon a locally optimal solution.

For an impulsive thrust case, the NLP has nine control decision variables: half transfer time $t_{1/2}$, forward coast time $t_{c,f}$, backward coast time $t_{c,b}$, forward arc velocity angle θ_f, forward arc velocity magnitude $|v|_f$, mid-course velocity angle θ_m, mid-course velocity magnitude $|v|_m$, backward arc velocity angle θ_b, and backward arc velocity magnitude $|v|_b$. Table 5.2 lists these decision variables in a concise reference table later in section 5.3.1. The solution is considered

feasible when the states of the forward and backward arcs match where they meet within a desirable tolerance. The cost function $f(\bar{x})$ is the change in velocity for all three burns. An optimal solution will reduce the midcourse burn to zero.

These trajectories tend to be very sensitive to initial conditions. Poor initial conditions may not converge to a solution at all. Additionally, the bounded solution space may have multiple local optimal solutions where one is more optimal than the rest. To enable SNOPT to find the more optimal solution, a numerical technique to push initial conditions out of locally optimal "wells" is needed.

5.1.2.1 Monotonic Basin Hopping

Monotonic basin hopping (MBH) allows an NLP to explore a bounded state space in a stochastic way. MBH picks a random initial guess $\bar{x}$ based on a user defined distribution such as Uniform, Gaussian, or Cauchy (this work is done with Uniform). SNOPT executes with this initial guess. If SNOPT does not converge to a solution then the initial guess is removed and MBH picks a new guess at random within the predefined bounds. If SNOPT converges to a feasible solution $\bar{x}^*$ then MBH will apply a random perturbation to the converged solution, called a "hop", and pass the perturbed solution back to SNOPT to resolve. If the perturbed solution performs better than the previous solution, the old solution is discarded and MBH hops from the new solution again. If the perturbed solution is infeasible or worse than the previous solution, then the perturbed solution is discarded and MBH hops in a different direction from the previous solution and a stagnation counter is iterated. If the stagnation counter exceeds a threshold, MBH resets the process with a new random guess. This step is important to hop out of local minimum pockets and better search the design space. MBH runs until one of the following conditions is met: a) a defined number of iterations, or b) a computational time limit.

5.2 DyLAN

Figure 5.3 shows a block diagram that details DyLAN from a top-level overview.

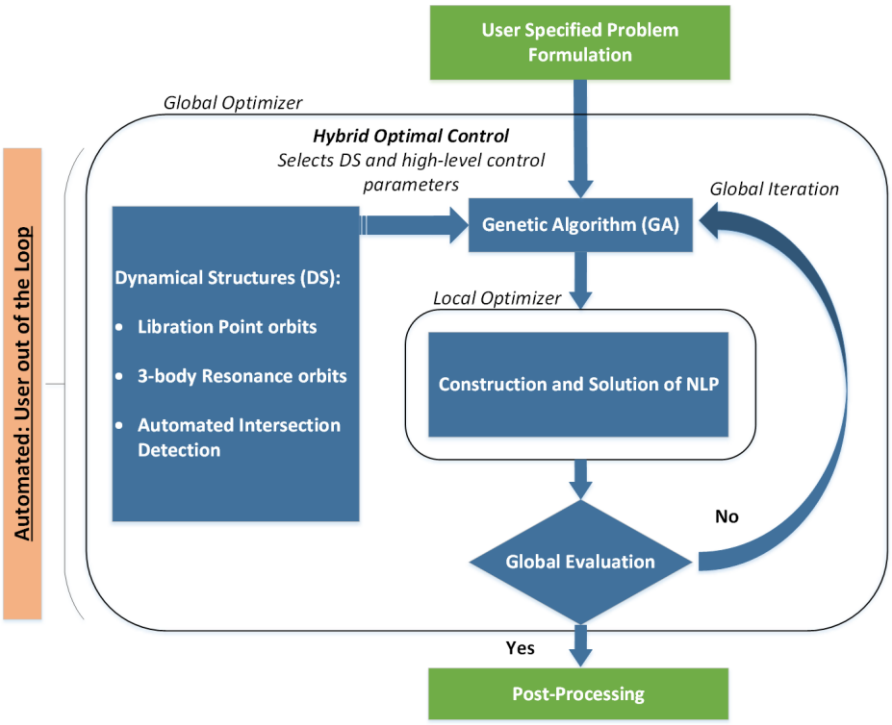

Figure 5.3 An overview of the optimization framework.

The program begins with the user defining the bounds on the problem such as initial and final conditions, bounds on orbit characteristics, and bounds on flight time. The outer loop GA is NSGA-II (Non-dominated Sorting Genetic Algorithm II), chosen for its ability to handle multiple objective optimization problems. The GA picks phase decision variables from different dynamical structures such as periodic orbits about Euler-Lagrange points or resonance orbits. The GA generates a population where each individual is a unique combination of phase decision variables within the user defined bounds. The phase variables define a two-point boundary value problem between parking orbits and dynamical structures which are solved for using the nonlinear program SNOPT. Once SNOPT closes the trajectory, the GA evaluates each individual based on the cost functions. This outer loop then inner loop cycle is repeated until the program converges to a family of solutions that form a trade space for the various cost functions. The user can then use these solutions to jumpstart their mission design by having access to a broad solution space.

Before the work presented here, DyLAN only had access to Lyapunov orbits and their respective manifolds to enable low-energy trajectory design. This included single-phase transfers, such as from an initial orbit to a Lyapunov parking orbit via a selected manifold or multi-phase transfers where Lyapunov orbits and their manifolds are linked together to achieve a longer sequence of transfers [50].

5.3 Augmentation for Resonance Structure

While DyLAN originally could only manipulate sequences of Lyapunov orbits and their manifolds, augmenting it with resonance-based dynamical structures significantly expands the design space. Including resonance orbits and their manifolds requires identifying key decision variables that the GA needs to be able to utilize sufficiently explore the design space.

5.3.1 Decision Variables for Hybrid Optimal Control

Resonance orbits are added to the framework by giving the outer loop six decision variables that characterize the orbit and manifold pair. Recall that with two-body approximation, multiple shooting, and parameter continuation that p, q, and r are sufficient to define the initial state of the resonance orbit along the x-axis (4.1.1). Additionally, the normalized time units τ_1 and τ_2 define the time along the resonance orbit before being perturbed and the time along the perturbation (manifold arc) respectively. These time parameters are sufficient at characterizing the invariant manifold off the resonance orbit. This is true for both a stable or unstable manifold arc, the only difference is the direction of perturbation. w is the direction of perturbation. Recall Figure 2.6 which shows two directions for both the stable and unstable arcs. For the purposes of this work, these two directions will be denoted “towards the primary” or towards the negative x-axis, with a p subscript, and “towards the secondary” or towards the positive x-axis, with a s subscript. Table 5.1 summarizes these decision variables.

Table 5.1 List of decision variables for the outer loop of DyLAN.

Variable	Description	Lower Bound	Upper Bound
$p:q$	Discrete resonance ratios Figure 4.5	Ratios found in Figure 4.5	
r	Nondimensionalized distance on the x-axis from the origin for initial condition	0.15	0.95
τ_1	Normalized time along the periodic orbit before perturbation	0.0	1.0 (Full period)
τ_2	Normalized time along the periodic orbit after perturbation	1.0	60.0 (260.556 days)
w	Direction of perturbation: towards the primary or secondary body; a discrete variable	w_p	w_s

The bounds of these decision variables will be shifted depending on the target mission. The NLP has nine decision variables for impulsive thrust case denoted in Table 5.2. The upper bound values are represented with their normalized values along with the dimension values in parenthesis.

Table 5.2 List of decision variables for the inner loop NLP.

Variable	Description	Lower Bound	Upper Bound
$t_{1/2}$	Half transfer time for each forward and backward arc	0.0	15.0 (65.139 days)
$t_{c,f}$	Forward coast time	0.0	3.0 (13.029 days)
$t_{c,b}$	Backward coast time	0.0	3.0 (13.029 days)
θ_f	Forward arc velocity angle	0.0	2π
$\lvert v\rvert_f$	Forward arc velocity magnitude	0.0	5.0 (5.123 km/s)
θ_m	Mid-course velocity angle	0.0	2π
$\lvert v\rvert_m$	Mid-course velocity magnitude	0.0	5.0 (5.123 km/s)
θ_b	Backward arc velocity angle	0.0	2π
$\lvert v\rvert_b$	Backward arc velocity magnitude	0.0	5.0 (5.123 km/s)

Chapter 6 details a few sample missions of resonance orbits in a HOC framework.

Chapter 6 SAMPLE TRAJECTORIES

This Chapter demonstrates the capabilities of DyLAN with a few simple trajectories focusing on trajectories enabled by resonance orbits. Three missions are explored here in detail. The first mission is a LEO to a cislunar resonance transfer. The second mission is a resonance to resonance orbit transfer with open r decision variable and the third mission is a resonance to resonance transfer with both r parameters held fixed.

6.1 LEO to Resonance Transfer

The first mission is a single-phase trajectory from a circular low Earth orbit to any cislunar resonance orbit. The initial parking orbit is 800 km, and the bounds on the genetic algorithm orbits are as follows:

Table 6.1 GA decision variable bounds for a LEO to resonance trajectory.

T_{orbit}	[0, 0.069] Days along the LEO orbit
$p{:}\,q$	1:1, 1:2, 1:3, 1:4, 2:3, 3:1, 3:4
r	0.85 Normalized dimension (fixed)
τ_1	[0, T_{reso}] Normalized time depending on ratio
τ_2	[0, 60] Normalized time units
w	w_p or w_s: Direction for stable manifold

Table 6.1 lists the types of resonance ratios that will be considered for this mission. These are a subset of the ones which were found and labeled in Figure 4.5. The radial distance is fixed and was chosen to be close to the moon to be similar to a L1 Lyapunov manifold transfer. The time variables were bounded such that τ_1 could be any time along the periodic orbit and τ_2 was chosen to be a substantially long time such that the manifold had sufficient time to flow away from the resonance orbit. The directional variable is a binary option which chooses the direction off the periodic orbit. T_{orbit} is the time along the LEO from an initial state on the positive x-axis (0° true anomaly). Using the decision variables in Table 5.2, the NLP is tasked with solving a TPBVP between the 800 km parking orbit and the state of the spacecraft at the end of the stable manifold arc.

The GA uses these decision variables to spawn a generation of 48 individuals. The algorithm is then executed iteratively for 90 generations. The generation history is compared to approximate the amount of change per generation. If the change between the 89th and 90th generation is significant then the algorithm is run for more generations. The following figures (Figure 6.1 and Figure 6.4) show the Pareto front of the final generation as well as a sample trajectory from the solution set.

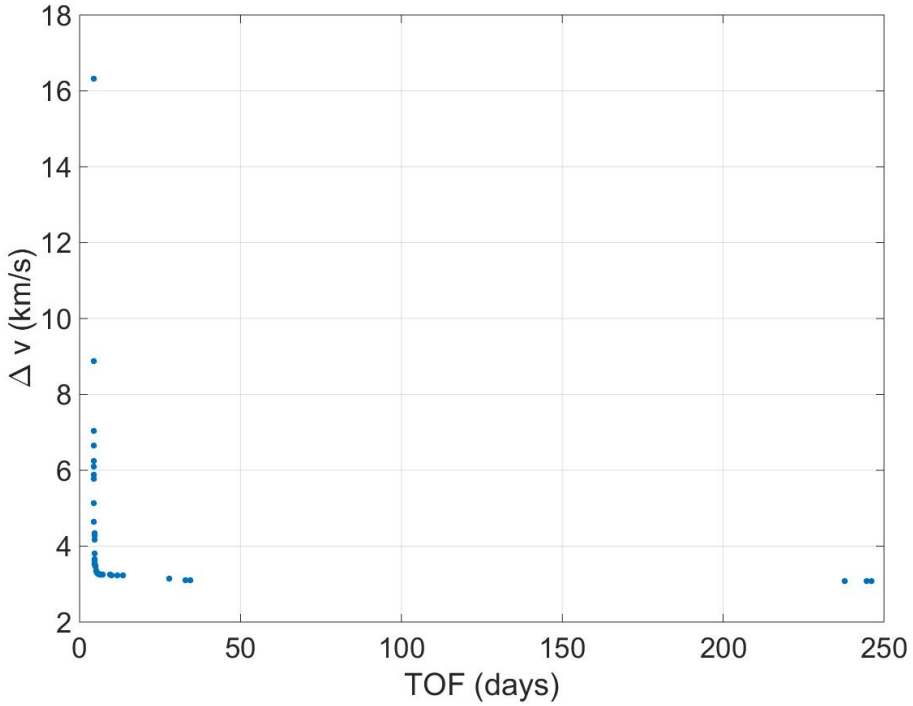

Figure 6.1 Pareto front of LEO to resonance transfer.

Figure 6.1 shows a sharply defined solution set. The trade space shows very little improvement in time of flight for drastic increases in fuel consumed. Similarly, there is hardly any improvement in fuel saved for drastic increases in time of flight. This solution set provides an array of trajectories that the astrodynamicist can choose the transfer which best suits the needs of the mission. If the mission requires a short time of flight then the astrodynamicist can compromise a bit of fuel for reduced flight time. Or, the mission designer may want a long tour of cislunar space before arriving at the parking orbit and therefore a long time of flight mission is desirable. Figure 6.2 shows the Pareto front zoomed in on the multi-objective corner where trajectories have both short time of flights and low fuel consumption.

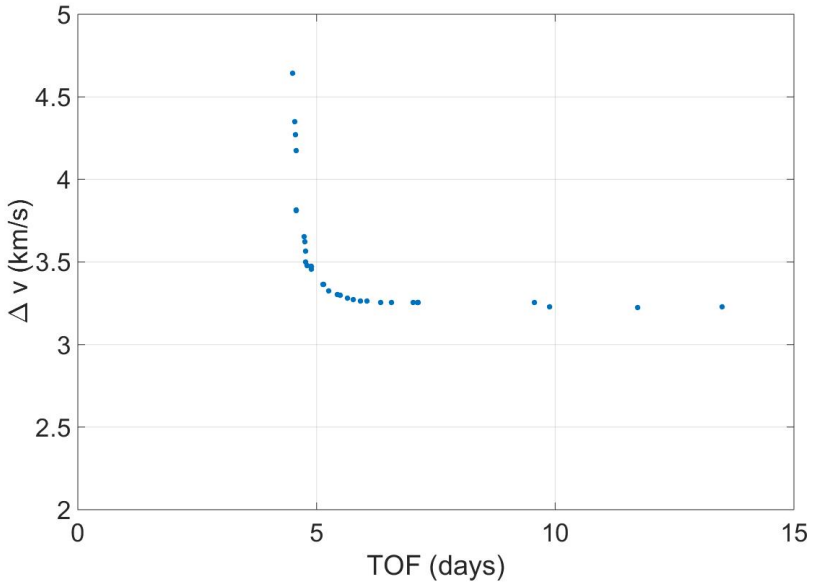

Figure 6.2 Close up of Figure 6.1.

Figure 6.3 shows the evolution of the Pareto front for multiple generations. The individuals conform quickly from a scattered set in the 5th generation to a clean front by the 50th generation. After the 50th generation the individuals transition from a spread across minimum fuel solutions to a spread across minimum time of flight solutions by the 90th generation.

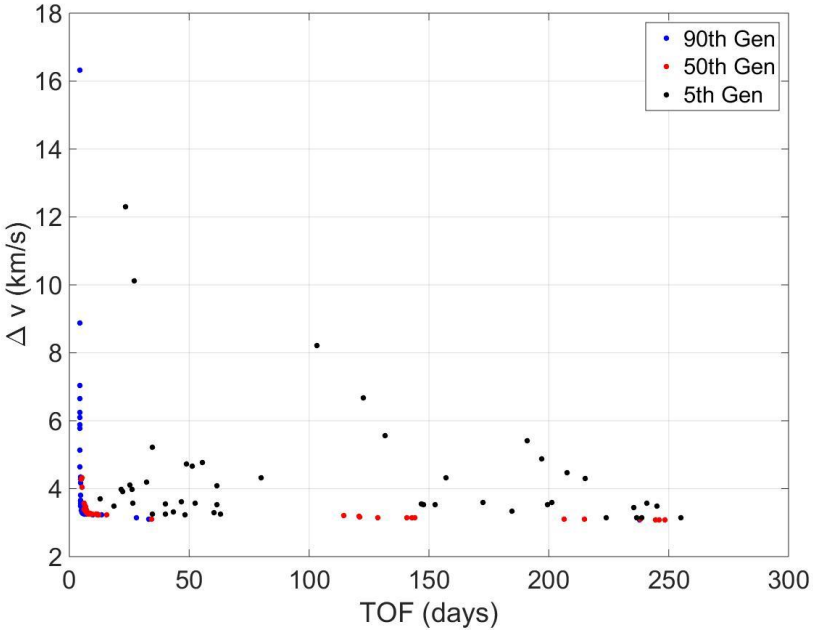

Figure 6.3 Evolution of Pareto front over generations in the GA

To better illustrate the various stages of the trajectory, the minimum Δv solution from the Pareto front will be used. This trajectory was chosen because it is an exaggerated example of how manifolds can be used in low-energy trajectory design. The trajectory requires a Δv of 3.076992 km/s and a transfer time of 246.13 days. The trajectory can be seen in Figure 6.4; it is a transfer from a 800 km circular LEO orbit to a 3:1 resonance orbit at $r = 0.85$. Figure 6.5 shows a series of steps along the trajectory. Step (a) shows the initial coast along the parking orbit, the length of which is determined by variable T_{orbit} which is chosen by the GA. Steps (b) - (d) detail the TPBVP transfer which is determined by the NLP decision variables. Steps (e) and (f) detail getting onto the stable resonance manifold and then final parking orbit which are determined by the final parking orbit variables p: q, r, τ_1, τ_2, and w which are chosen by the GA.

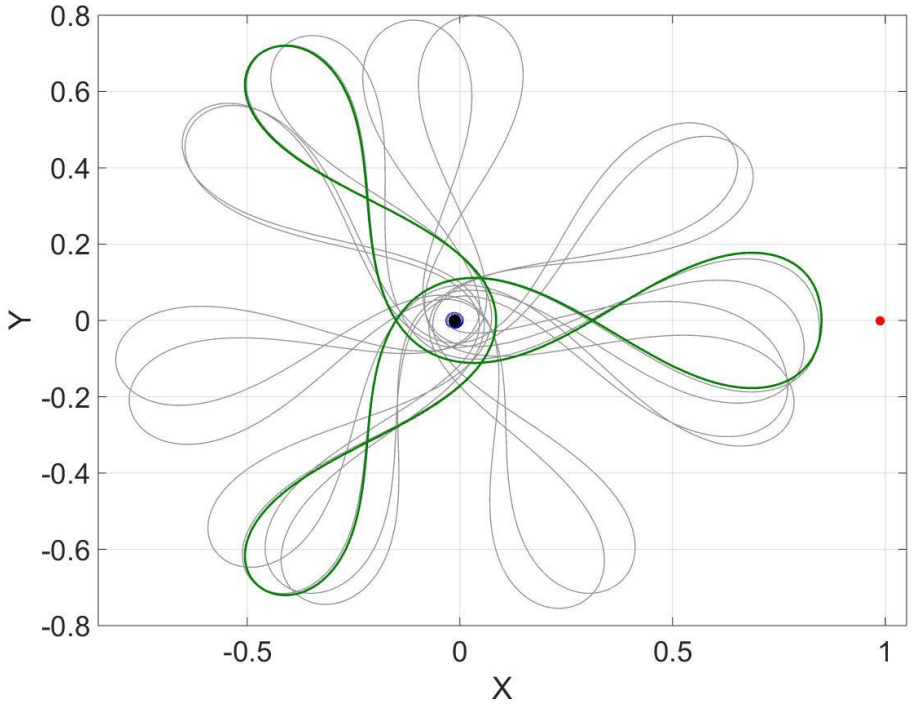

Figure 6.4 Minimum fuel LEO to cislunar resonance trajectory from solution set.

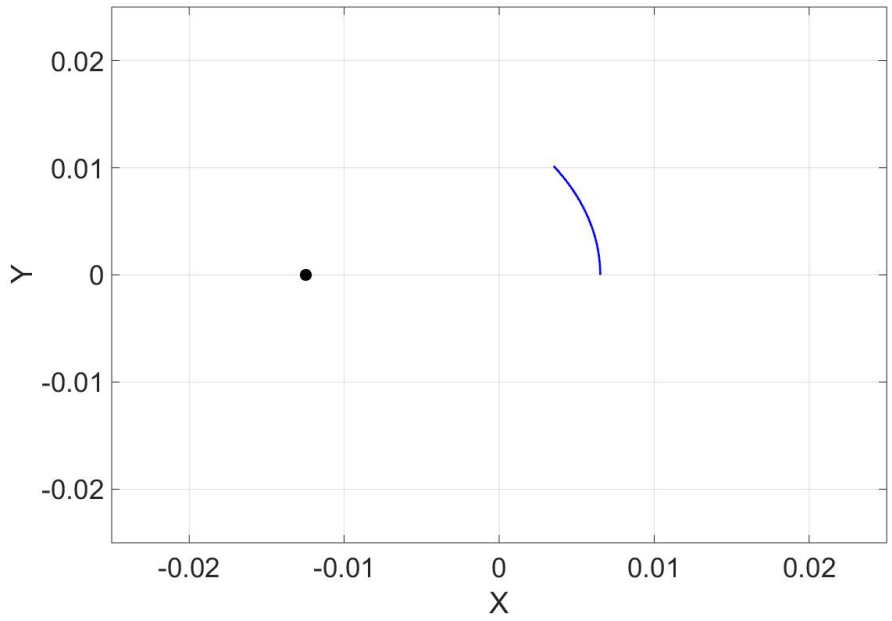

(a) The spacecraft departs from its initial state at LEO and coasts for T_{orbit} time units.

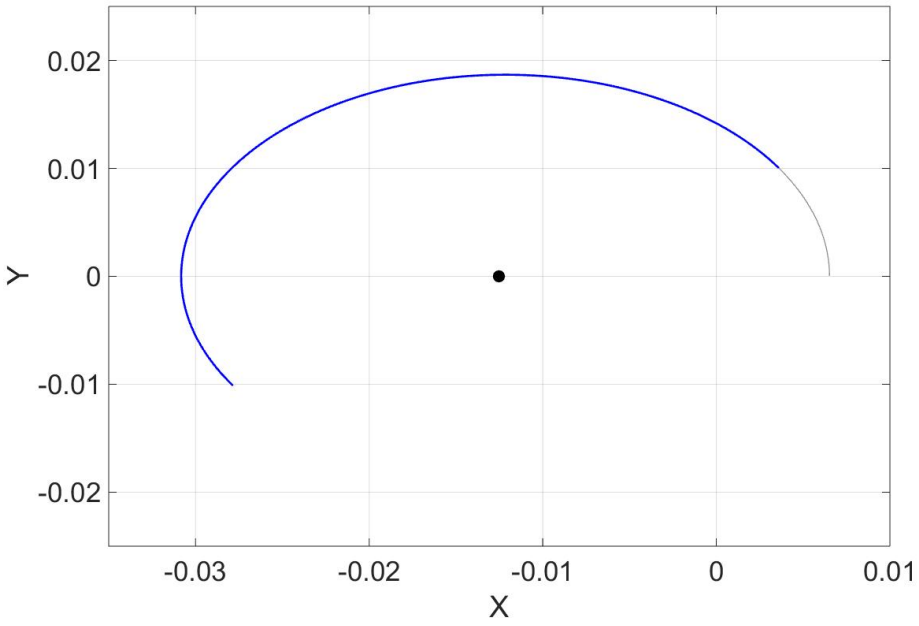

(b) The spacecraft coasts along the initial LEO parking orbit for $t_{c,f}$ time units.

Figure 6.5 LEO to resonance trajectory broken into discrete steps (a)-(f).

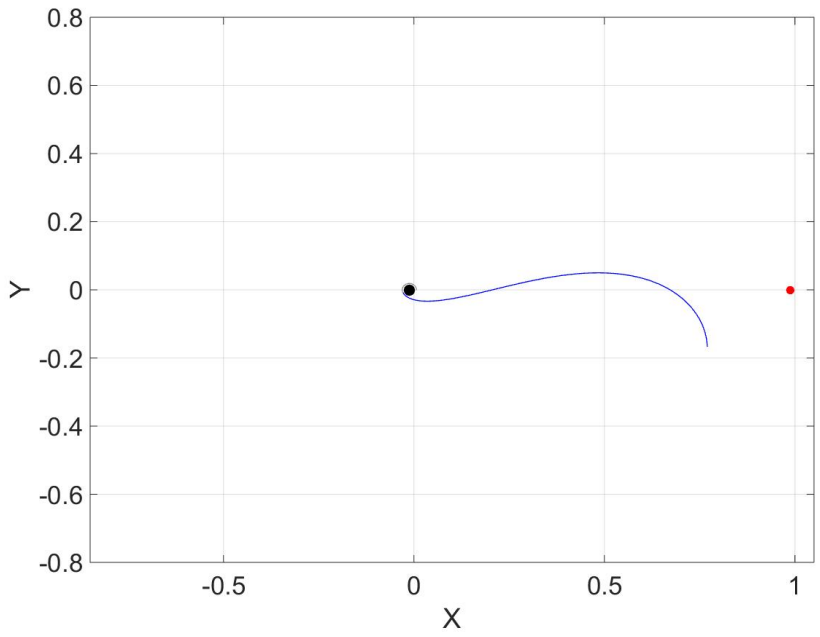

(c) The spacecraft performs a burn and coasts for $2t_{1/2}$ time units before performing the second and final burn. Note the change in scale, and thus relative invisibility of the original parking orbit.

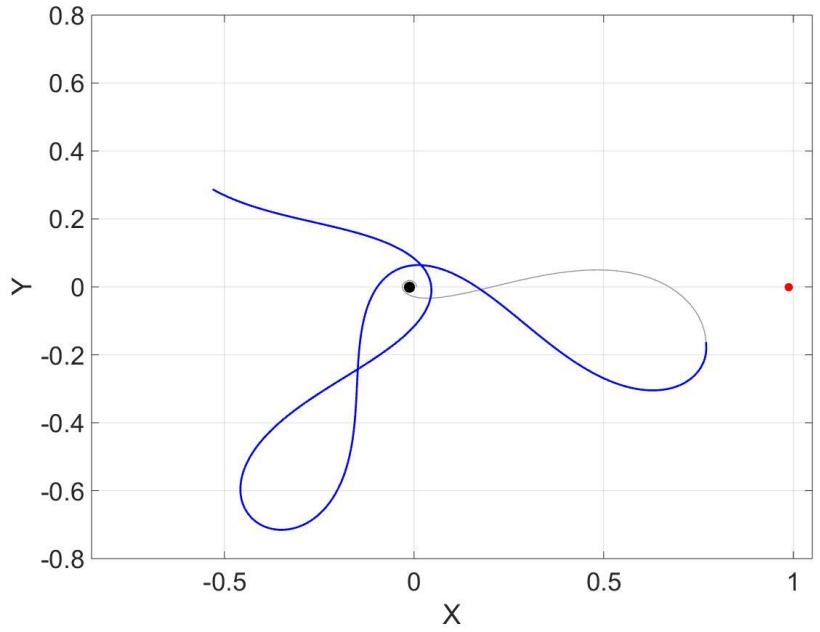

(d) The spacecraft coasts an additional $t_{c,b}$ time units. This is a decision variable set by the NLP.

Figure 6.5 Continued.

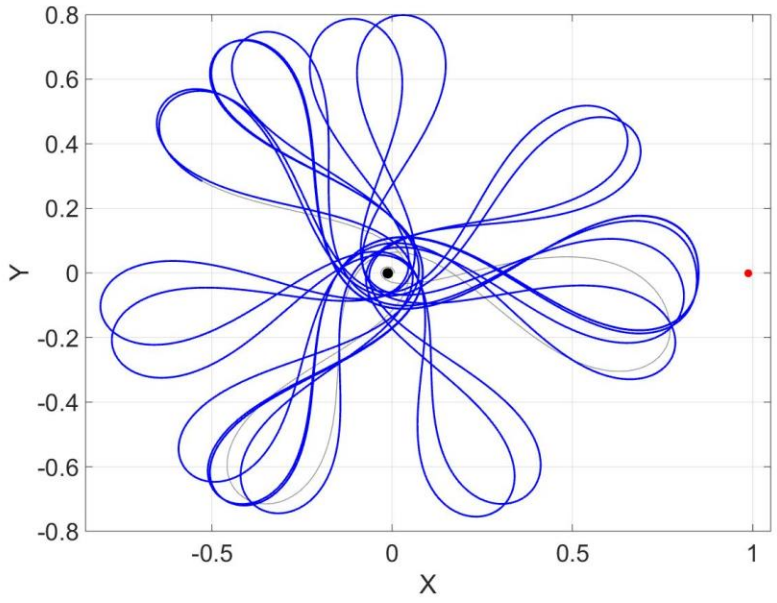

(e) The spacecraft coasts onto the stable manifold arc and then coasts along the arc for a prescribed τ_2 time along the arc.

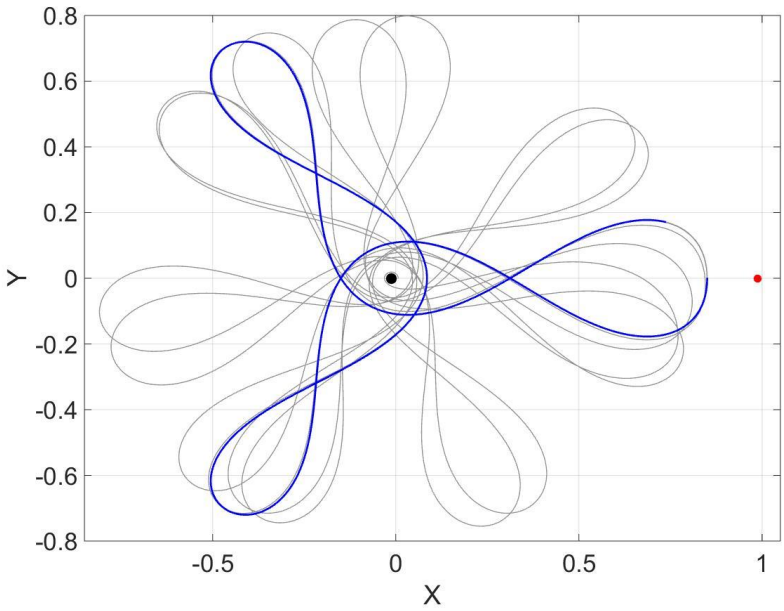

(f) The spacecraft performs another miniscule burn, in the w_p direction, off the manifold and onto the periodic orbit. The spacecraft then coasts for τ_1 time units bringing it back to its original state on the x-axis. The spacecraft is now on the final 3:1 parking orbit.

Figure 6.5 Continued.

Table 6.2 shows all the final decision variable values for the specific trajectory shown in Figure 6.4. Listed are the decision variables for the GA as well as the decision variables for the NLP.

Table 6.2 Final GA and NLP decision variables for LEO to 3:1 resonance transfer.

Variable	Value (Normalized Units)
T_{orbit}	0.00146913
$p: q$	3:1
r	0.85* fixed
τ_1	5.85681
τ_2	53.142589
w	w_p
$t_{1/2}$	0.382136
$t_{c,f}$	0.00808
$t_{c,b}$	3.14499
θ_f	5.2812315
$\|v\|_f$	2.8922
θ_m	5.084716136
$\|v\|_m$	0.0
θ_b	4.48221
$\|v\|_b$	0.11115

6.2 Resonance to Resonance Transfer: Open R

The purpose of demonstrating the resonance to resonance mission with an open R target is to validate the search process of the outer loop. The mission is to transfer from any resonance orbit to another. In order to minimize the cost functions, particularly Δv, the algorithm should naturally converge on solutions where each resonance pair has the same p, q, and r decision variables. This is equivalent to saying the most fuel efficient transfer is to simply stay at the initial conditions. Table 6.3 denote the bounds on the decision variables initially introduced in Table 5.1 for this

specific mission. Since both the initial and final parking orbit are resonance orbits they will each have an invariant manifold arc. To distinguish these similar variables the initial parking orbit will be generated from $p_1: q_1$ and r_1 and will have an unstable manifold off of it defined by the time variables $\tau_{1,US}$ and $\tau_{2,US}$ where the subscript US indicates that it belongs to the unstable manifold arc. Conversely the final parking orbit will have a stable manifold onto the orbit so the manifold variables will be denoted with an S subscript. Bracketed values indicate a continuous range while the others are discrete decision variables.

Table 6.3 Decision variables for a resonance to a resonance transfer.

$p_1: q_1$	1:1, 1:2, 1:3, 1:4, 2:1, 2:3, 3:1, 3:2, 3:4, 4:1
$p_2: q_2$	1:1, 1:2, 1:3, 1:4, 2:1, 2:3, 3:1, 3:2, 3:4, 4:1
r_1, r_2	[0.35, 0.65]
$\tau_{1,US}$	[0, T_{reso1}]
$\tau_{1,S}$	[0, T_{reso2}]
$\tau_{2,US}, \tau_{2,S}$	[0, 60] for both
w_{US}, w_S	$w_{US,p}$or $w_{US,s}$ & $w_{S,p}$ or $w_{S,s}$

After 90 generations the solution space has conformed to the following solution front:

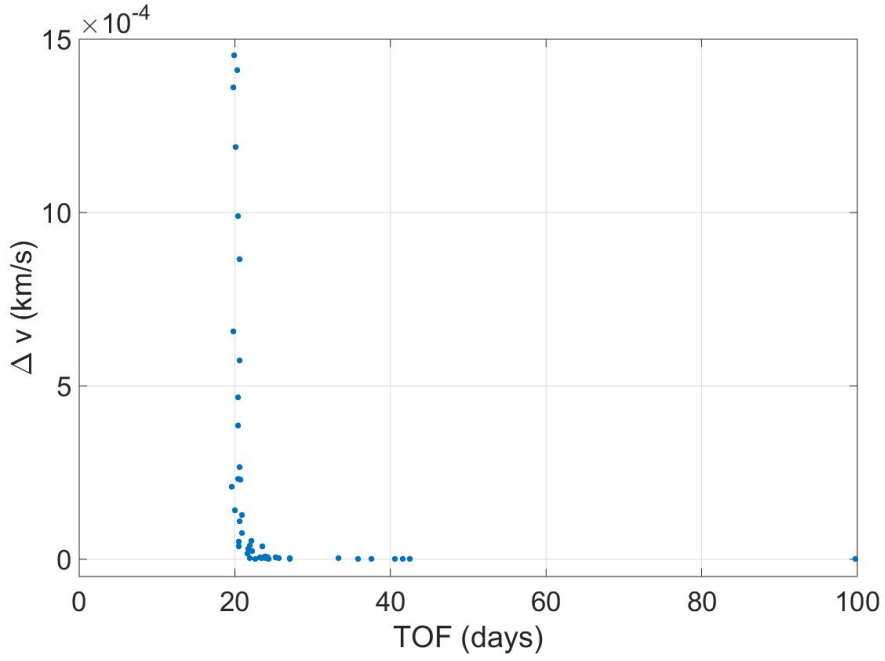

Figure 6.6 Resonance to resonance Pareto front.

The solution front conforms to a tight set of solutions with a miniscule Δv for a range of time of flights. Figure 6.8 shows a sample trajectory from the solution set. As predicted, the GA converged towards solutions where resonance ratio and position were the same such that the "transfer" is truly minimum in that the spacecraft never leaves the orbit it begins on. This gives confidence that DyLAN is capable of searching a large design space with multiple decision variables in both the GA and NLP and still arrive at the logical solution. The Pareto front settled to this distribution early in the evolutionary process. It did not take many generations for the individuals to converge to the solution front seen in Figure 6.6. Figure 6.7 shows the evolution of individuals at discrete points. The individuals at the 5th generation are quite scattered and not converged to a solution front. However, by the 50th generation most of the individuals are settled into a solution front with only minor modifications until the tool terminates at the 90th generation.

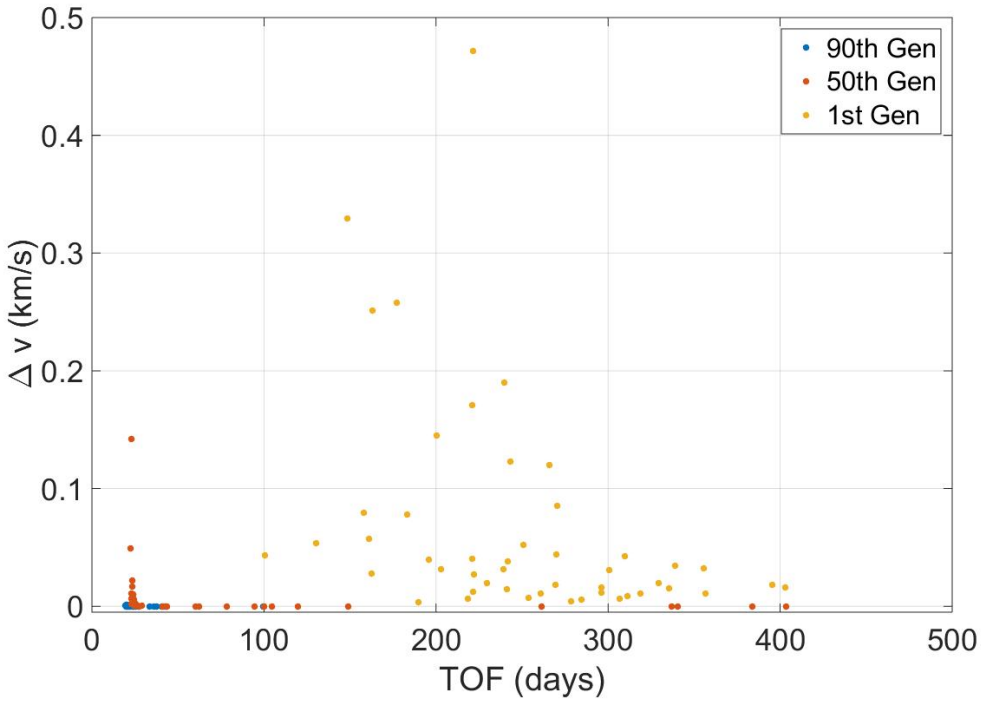

Figure 6.7 Evolution of Pareto front over generations in the GA

The chosen sample trajectory is the multi-objective minimal case. The trajectory requires a Δv of 1.511E-6 km/s and a transfer time of 35.85 days. The trajectory can be seen in Figure 6.8, as a transfer from a 1:1 resonance to a 1:1 resonance at equal r values as predicted. Figure 6.9 shows a series of steps along the trajectory. Steps (a) and (b) are determined by the initial parking orbit

variables p_1, q_1, r_1, $\tau_{1U,S}$, $\tau_{2,US}$, and w_s which are chosen by the GA. Steps (c) and (d) detail the TPBVP transfer which are determined by the NLP decision variables. Steps (e) and (f) are determined by the final parking orbit variables p_2, q_2, r_2, $\tau_{1,S}$, $\tau_{2,S}$, and w_u which are also chosen by the GA. . Note that resonance orbits are much more stable than common low-energy transfer orbits such as Lyapunov orbits about Euler-Lagrange points. This means that when a spacecraft performs a small maneuver to get onto a manifold arc, the manifold often follows very closely to the original periodic orbit. This is particularly prevalent in steps (e) to (f) when the spacecraft transitions from the stable manifold of the final parking orbit to the final parking orbit itself. Notice that the spacecraft travels back in the direction of the manifold and that the minor burn performed is sufficient to keep the spacecraft along the 1:1 resonance orbit.

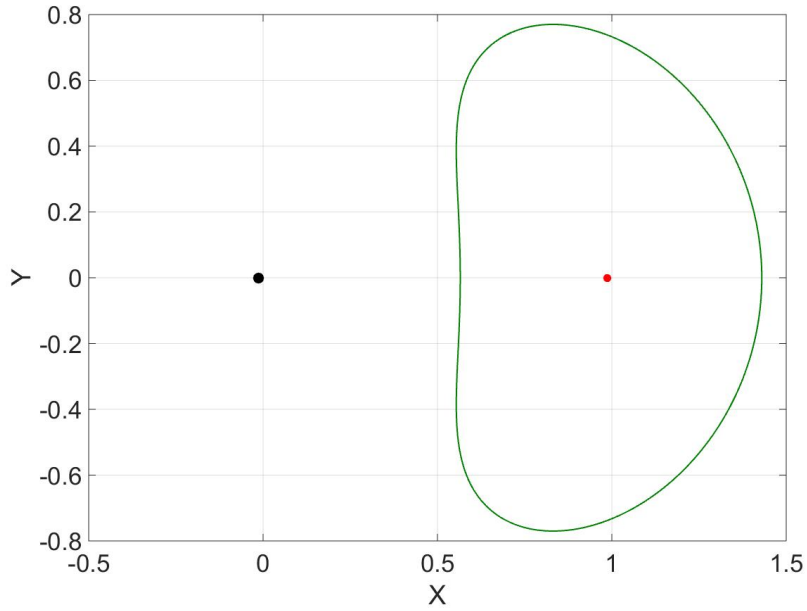

Figure 6.8 Resonance to resonance sample trajectory from the solution set. This is a 1:1 resonance to a 1:1 resonance. They are the same orbit.

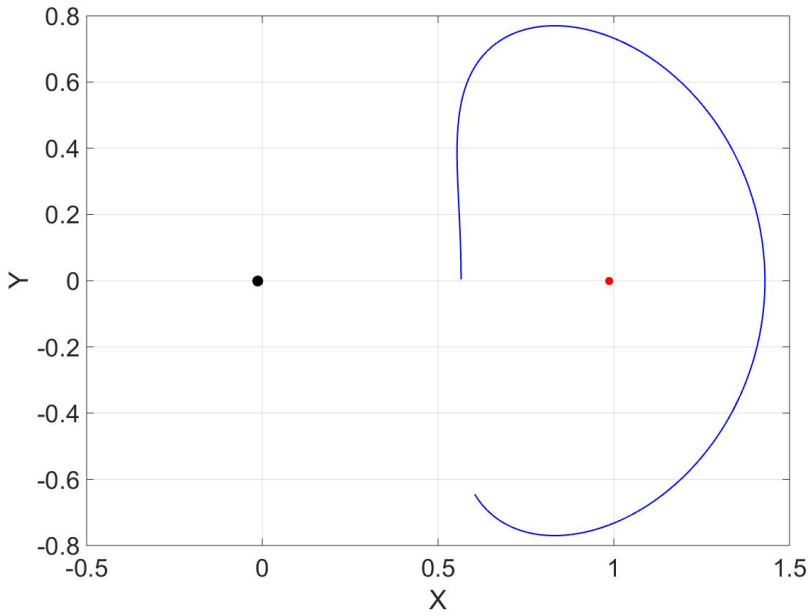

(a) Coast along the initial parking orbit a prescribed $\tau_{1,US}$ time units.

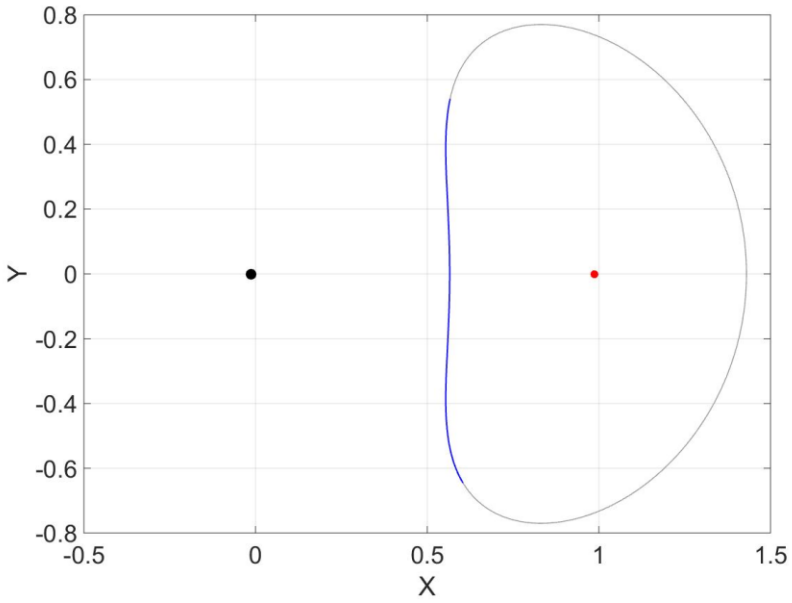

(b) The spacecraft performs a miniscule burn in the w_p direction to jump onto the unstable manifold and coasts for $\tau_{2,US}$ time units.

Figure 6.9 Trajectory broken into discrete steps (a)-(g).

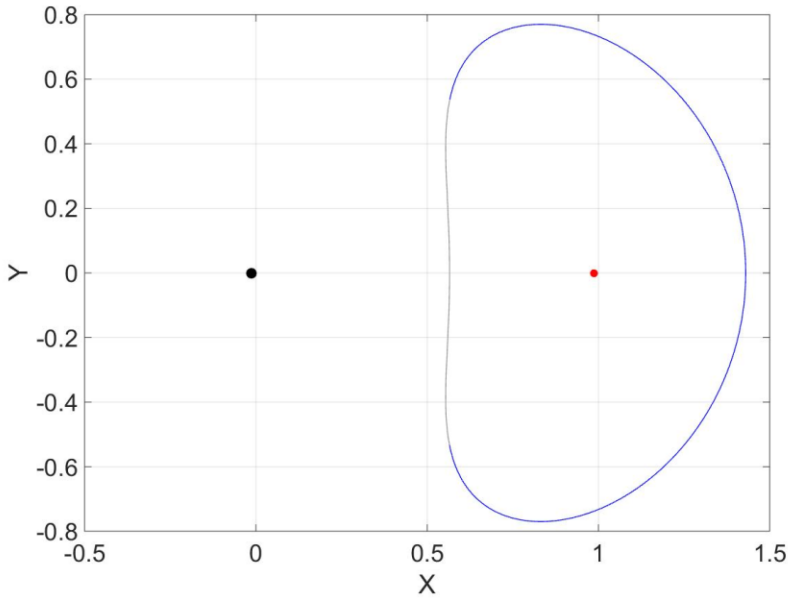

(c) The spacecraft performs a burn and coasts for $2t_{1/2}$ time units before performing the second and final burn ($t_{c,f} = 0$).

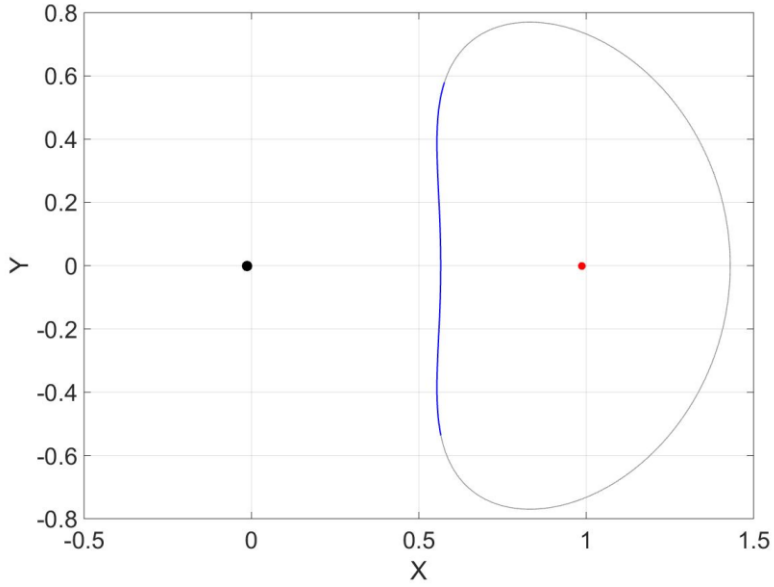

(d) The spacecraft coasts an additional $t_{c,b}$ time units. This is a decision variable set by the NLP.

Figure 6.9 Continued.

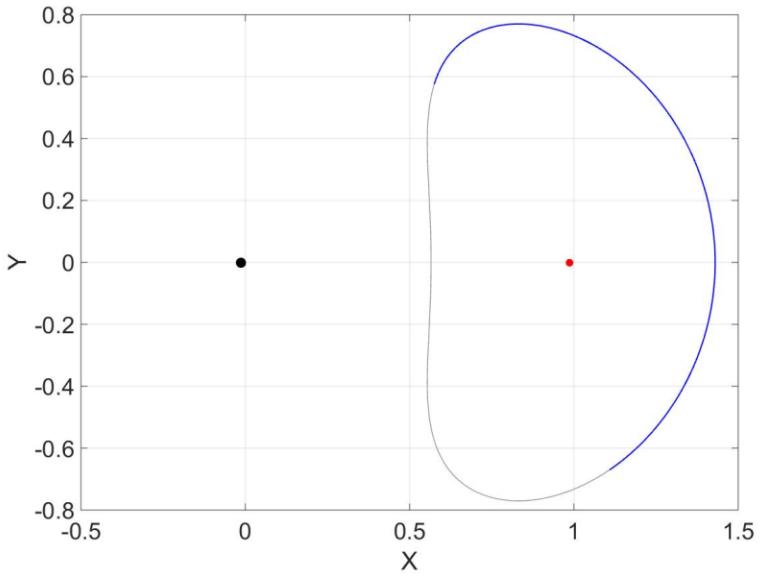

(e) The spacecraft coasts onto the stable manifold arc and coasts an additional $\tau_{2,S}$ time units along the arc.

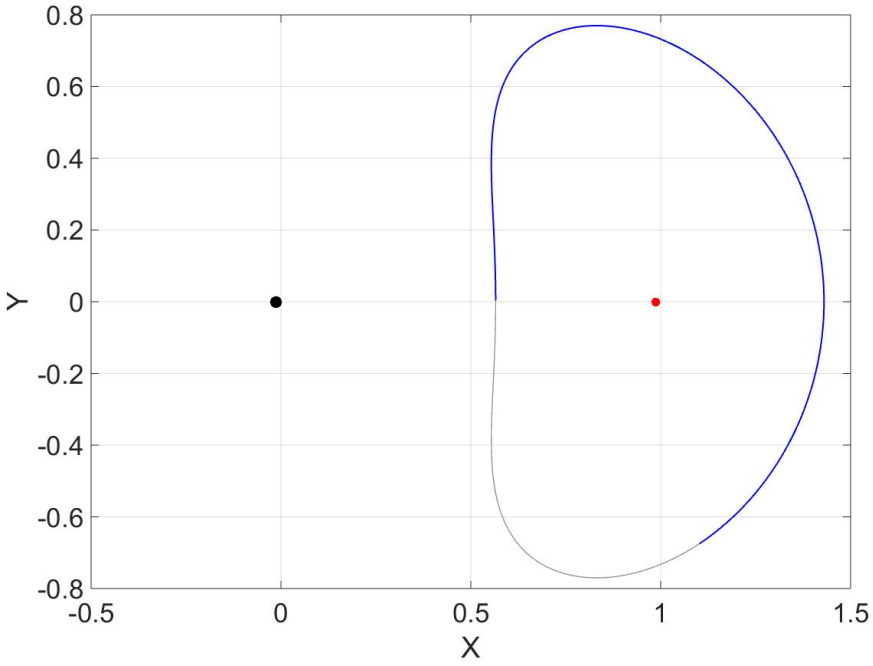

(f) The spacecraft performs another miniscule burn, in the w_p direction, off the manifold and onto the periodic orbit. The spacecraft then coasts for $\tau_{1,S}$ time units bringing it back to its original state on the x-axis. The spacecraft is now on the final 1:1 parking orbit.

Figure 6.9 Continued.

Table 6.4 shows all the final decision variable values for the specific trajectory shown in Figure 6.8. Listed are the decision variables for the GA as well as the decision variables for the NLP.

Table 6.4 Final GA and NLP decision variables for 1:1 to 1:1 transfer.

Variable	Value (Dimensionless)
$p_1 : q_1$	1:1
r_1	0.56534053971
$\tau_{1,US}$	0.85349786144
$\tau_{2,US}$	1.48334723722
w_{US}	$w_{US,p}$
$p_2 : q_2$	1:1
r_2	0.56533029768
$\tau_{1,S}$	0.672379646819
$\tau_{2,S}$	3.18009249908
w_S	$w_{S,p}$
$t_{1/2}$	2.18838
$t_{c,f}$	0.0
$t_{c,b}$	1.4698
θ_f	1.68378
$\lvert v \rvert_f$	1.475E-6
θ_m	1.45
$\lvert v \rvert_m$	0.0
θ_b	0.461088
$\lvert v \rvert_b$	0.0

6.3 Resonance to Resonance Transfer: Targeted R

The purpose of this resonance to resonance mission is to demonstrate a more challenging transfer utilizing both stable and unstable manifolds. The mission is to transfer from a resonance orbit at $r = 0.25$ to another at $r = 0.95$. This displays DyLAN's ability to transfer from an elliptical orbit whose perigee is at 0.25 normalized units to an elliptical orbit whose perigee is at 0.95 normalized units using invariant manifolds. Table 6.5 lists the bounds on the decision variables initially introduced in Table 5.1 for this specific mission. Since both the initial and final parking orbit are resonance orbits they will each have an invariant manifold arc. Like the previous problem, to distinguish these similar variables, the initial parking orbit will be generated from $p_1 : q_1$ and r_1 and will have an unstable manifold off of it defined by the time variables $\tau_{1,US}$ and $\tau_{2,US}$ where the subscript US indicates that it belongs to the unstable manifold arc. Conversely the final parking orbit will have a stable manifold onto the orbit so the manifold variables will be denoted with an S subscript. Bracketed values indicate a continuous range while the others are discrete decision variables.

Table 6.5 Decision variables for a resonance to a resonance transfer.

$p_1 : q_1$	1:1, 1:2, 1:3, 1:4, 2:3, 3:1, 3:4, 4:1
$p_2 : q_2$	1:2, 1:3, 1:4, 2:3, 3:4
r_1, r_2	0.25 & 0.95 Fixed
$\tau_{1,US}$	[0, T_{reso1}]
$\tau_{1,S}$	[0, T_{reso2}]
$\tau_{2,US}, \tau_{2,S}$	[0, 60] for both
w_{US}, w_S	$w_{US,p}$ or $w_{US,s}$ & $w_{S,p}$ or $w_{S,s}$

Figure 6.10 shows the Pareto front of the individuals after 90 generations.

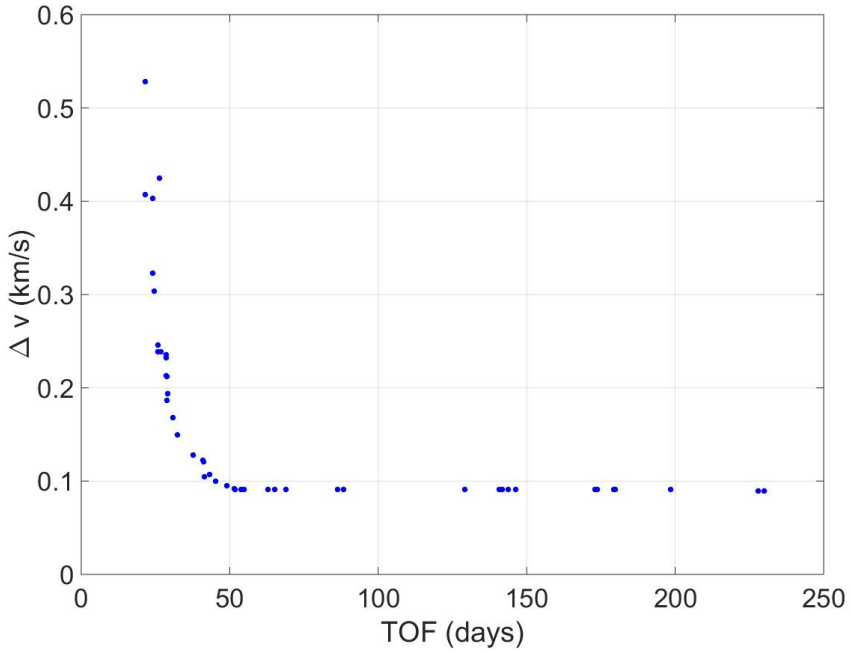

Figure 6.10 Resonance to resonance Pareto front.

The solution front conforms to a tight set of solutions with a miniscule Δv for a range of time of flights. Figure 6.12 shows a sample trajectory from the solution set. The Pareto front settled to this distribution early in the evolutionary process. It did not take many generations for the individuals to converge to the solution front seen in Figure 6.10. Figure 6.11 shows the evolution of individuals at discrete points. The individuals at the 5^{th} generation are moderately scattered, but a general concave structure is being formed. By the 50^{th} generation most of the individuals are settled into a solution front with only minor modifications until the tool terminates at the 90^{th} generation.

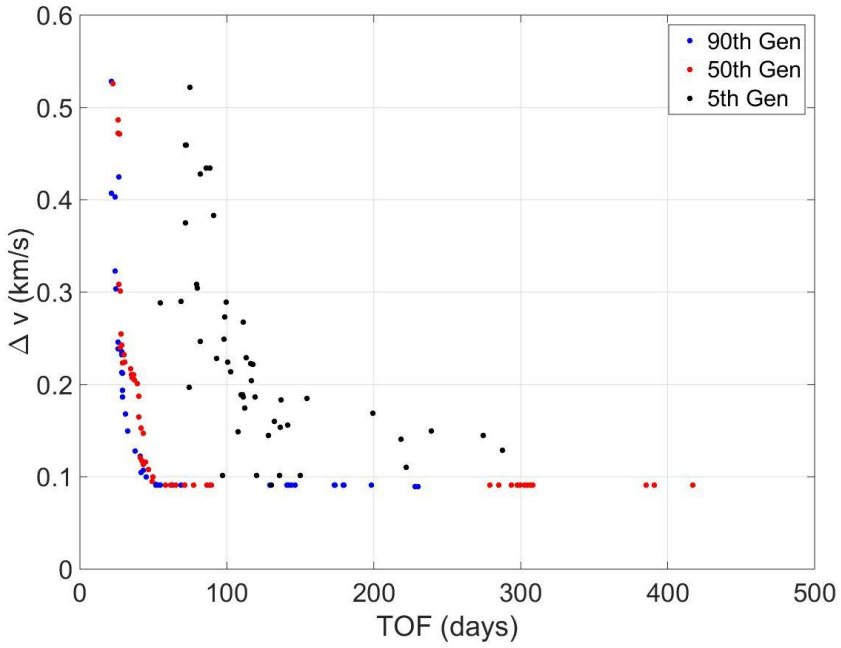

Figure 6.11 Evolution of Pareto front over generations in the GA

The chosen sample trajectory is the multi-objective minimal case. The trajectory requires a Δv of 0.09947 km/s and a transfer time of 62.855 days. The trajectory can be seen in Figure 6.12, as a transfer from a 3:4 resonance to a 1:4 resonance. Figure 6.13 shows a series of steps along the trajectory. Steps (a) and (b) are determined by the initial parking orbit variables p_1, q_1, r_1, $\tau_{1U,S}$, $\tau_{2,US}$, and w_s which are chosen by the GA. Steps (c) - (e) detail the TPBVP transfer which are determined by the NLP decision variables. Steps (f) and (g) are determined by the final parking orbit variables p_2, q_2, r_2, $\tau_{1,S}$, $\tau_{2,S}$, and w_u which are also chosen by the GA.

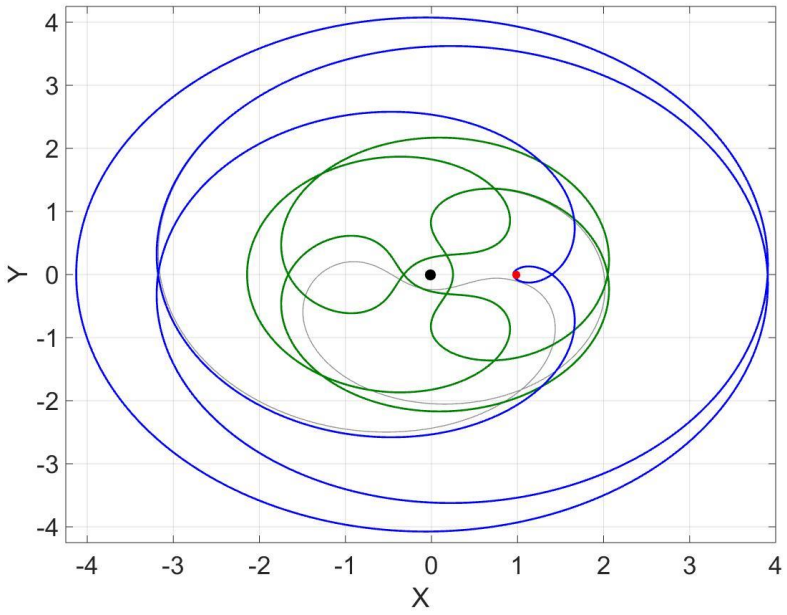

Figure 6.12 Resonance to resonance sample trajectory from the solution set. This is a 3:4 resonance to a 1:4 resonance.

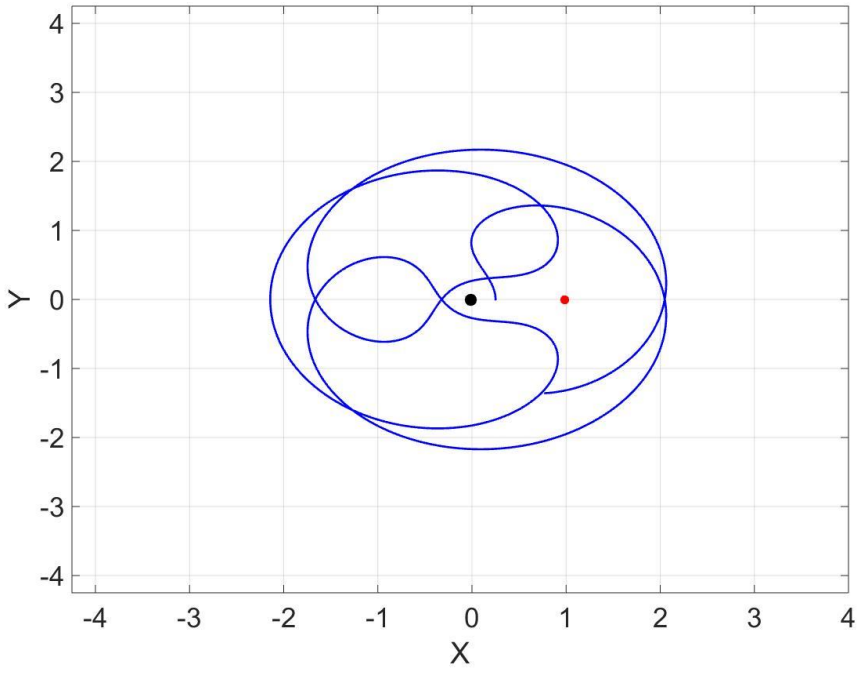

(a) Coast along the initial parking orbit a prescribed $\tau_{1,US}$ time units.

Figure 6.13 Trajectory broken into discrete steps (a)-(g).

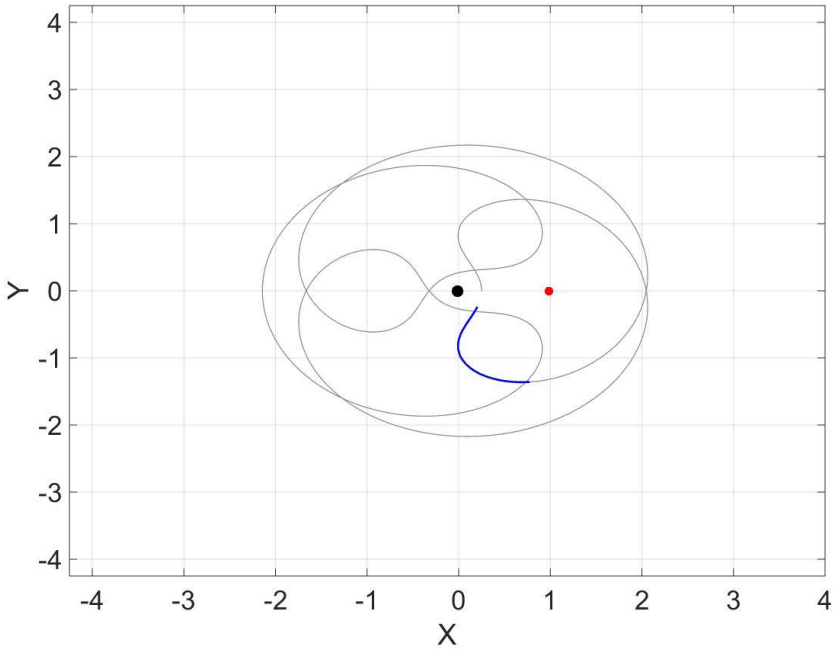

(b) The spacecraft performs a miniscule burn, in the w_s direction, to jump onto the unstable manifold and coasts for $\tau_{2,US}$ time units.

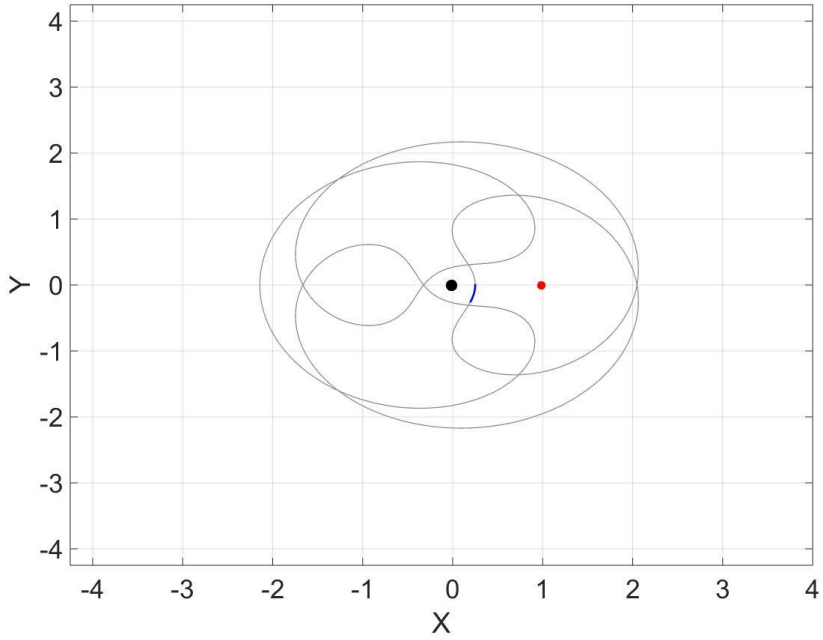

(c) The spacecraft coasts along the unstable manifold an additional $t_{c,f}$ time. This is a decision variable set by the NLP.

Figure 6.13 Continued.

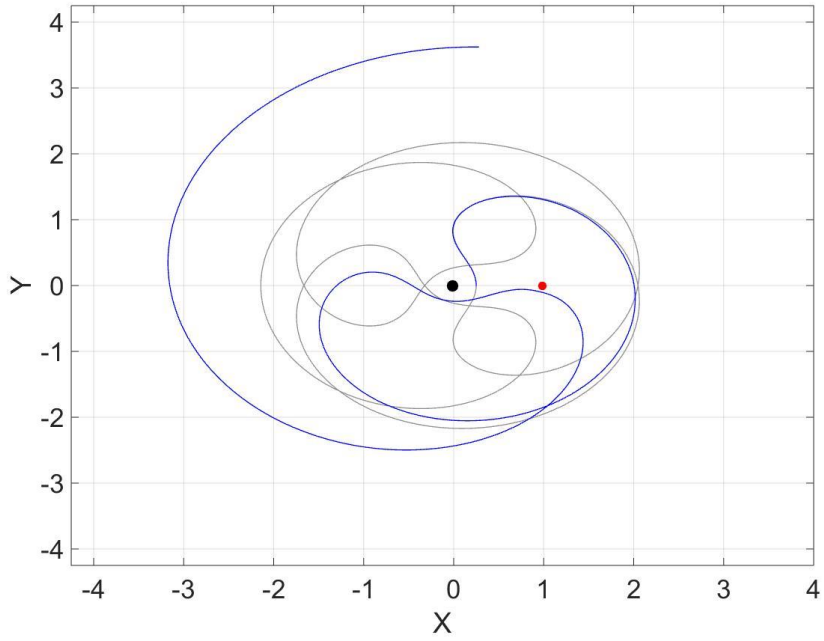

(d) The spacecraft performs a burn and coasts for $2t_{1/2}$ time units and then performs the second and final burn.

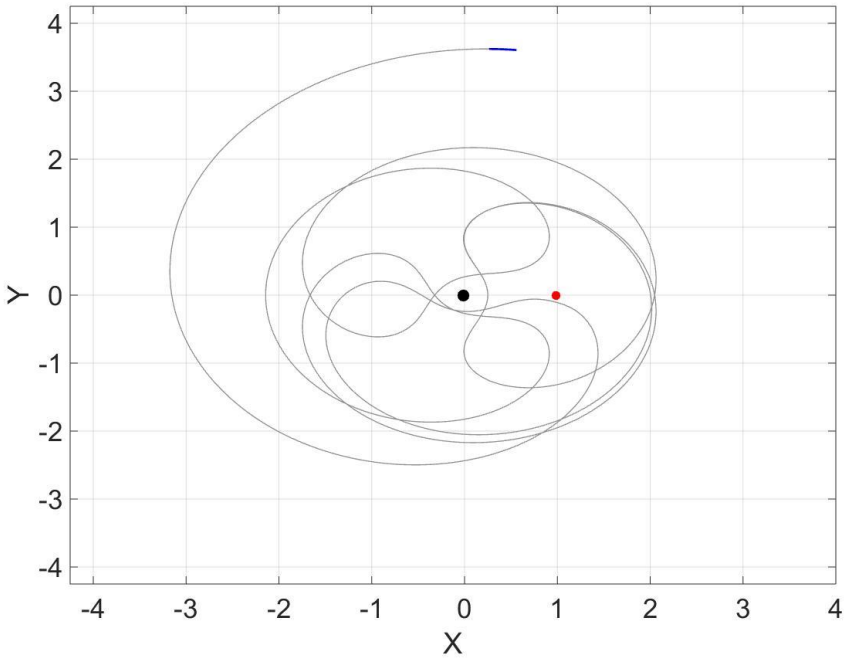

(e) The spacecraft coasts an additional $t_{c,b}$ time units. This is a decision variable set by the NLP.

Figure 6.13 Continued.

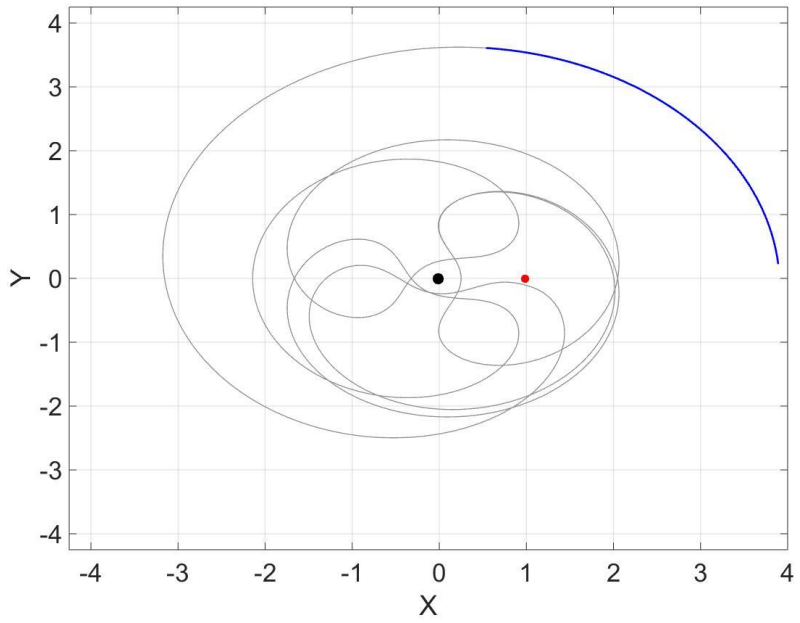

(f) The second burn jumps the spacecraft onto the stable manifold arc at the state associated with the prescribed $\tau_{2,S}$ time along the arc.

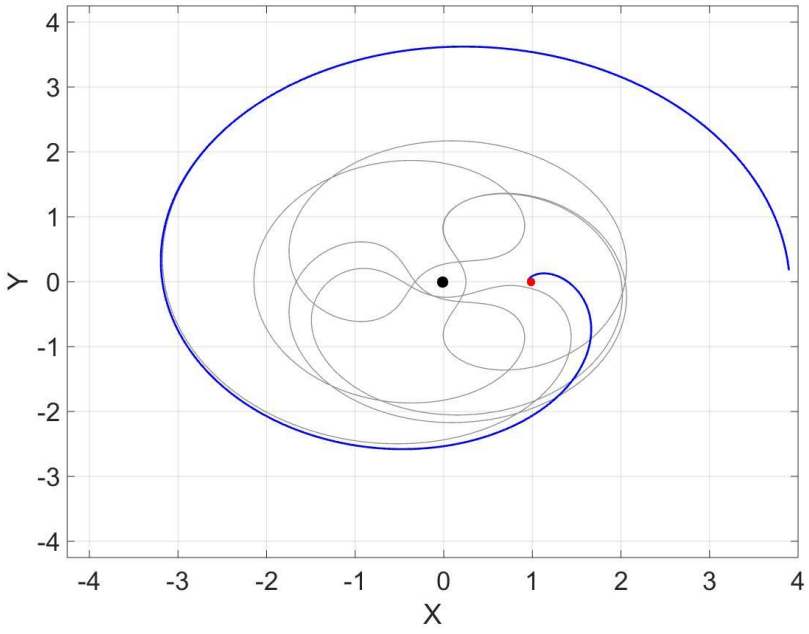

(g) The spacecraft performs another miniscule burn, in the w_s direction, off the manifold and onto the periodic orbit. The spacecraft then coasts for $\tau_{1,S}$ time units bringing it back to its original state on the x-axis. The spacecraft is now on the final 1:4 parking orbit.

Figure 6.13 Continued.

Table 6.6 shows all the final decision variable values for the specific trajectory shown in Figure 6.12. Listed are the decision variables for the GA as well as the decision variables for the NLP.

Table 6.6 Final GA and NLP decision variables for 3:4 to 1:4 transfer.

Variable	Value (Dimensionless)
$p_1 : q_1$	3:4
r_1	0.25 Fixed
$\tau_{1,US}$	0.935836151051
$\tau_{2,US}$	1.49687681126
w_{US}	$w_{US,s}$
$p_2 : q_2$	1:4
r_2	0.95 Fixed
$\tau_{1,S}$	0.354857685496
$\tau_{2,S}$	1.49671164469
w_S	$w_{S,s}$
$t_{1/2}$	7.23696854367
$t_{c,f}$	0.116277755424
$t_{c,b}$	0.0825358576926
θ_f	4.71183726357
$\lvert v \rvert_f$	0.00589127284335
θ_m	2.47815109481
$\lvert v \rvert_m$	0.0
θ_b	0.0
$\lvert v \rvert_b$	0.0911990450789

6.4 Summary of Results

The three missions detailed above show a range of missions that DyLAN is able to solve with resonance orbits and their manifolds incorporated into the hybrid optimal control algorithm. These missions, particularly the LEO to resonance and resonance to resonance with fixed r parameter, are of particular interest to the astrodynamicist community because they display low-energy means of touring cislunar space. In addition to the few shown trajectories, each mission was solved such that a trade space of solutions for the multi-objective Pareto front was provided all at once. All three of these missions took approximately 3.5 hours to run on a computer cluster of 48 processors, one for each individual to be computed embarrassingly parallel. Furthermore, these solutions were generated autonomously beyond a human bounding the decision variables. In summary, by using resonance dynamical structures in the DyLAN tool, a trade space of solutions to three different missions were generated autonomously in a computationally efficient manner in a way that has not been done before.

Chapter 7 CONCLUSIONS

7.1 Summary of Contributions

The work in this thesis extends previous work on trajectory design using resonance orbits. Vaquero [26] [27] [42] and Anderson [20] [21] [22] [24] [38] [44] have been particularly active in recent years studying resonance orbits in this manner. This work detailed incorporating resonance orbits into automated low-energy trajectory design in the three-body problem. Incorporating resonance orbits autonomously was done by two significant efforts. The first effort was to generate resonance orbits in a robust fashion. These orbit generation methods were automated and incorporated into the larger low-energy trajectory solver, DyLAN. The result was robust generation for a number of p: q ratios in three-body systems, and specifically demonstrated for both high (Jupiter-Europa) and low (Earth-moon) relative mass systems. This required implementing robust algorithms such as multiple shooting, radial continuation, and gravitational parameter continuation. The second effort, once robust generation was developed, was to incorporate the resonance dynamical structure into DyLAN's hybrid optimal control algorithm. This included identifying key parameters that define a resonance orbit and manifold and determining bounds for each decision variable that give the HOC algorithm a proper design space. This integration was tested in three basic missions: a LEO parking orbit to resonance orbit, a resonance to resonance transfer with open r decision variable, and a resonance to resonance transfer with fixed r values. These missions are examples of practical mission applications of the tool as they represent real trajectories of interest for cislunar missions.

This effort has some limitations in the types of trajectories it can produce. The techniques detailed here can cover a larger range of resonance orbits in the Jupiter-Europa system where the two-body approximation is more accurate. Unfortunately, the range of resonance ratios is reduced in the Earth-Moon system where the two bodies have much closer mass. Additionally, the range of the resonance families is limited. For example, most orbits detailed here are defined within $r \in [0.25, 0.95]$ normalized distance units on the x-axis. Notice this excludes orbits near both the primary, secondary, and beyond the secondary. Lastly, the work only details single-phase impulsive thrust missions but there is a significant potential in missions utilizing low-thrust

propulsion and multiple phases. These limitations are strong candidates for future work developing DyLAN and its utilization of resonance dynamical structures.

7.2 Future Work

Future work should be aimed at making the resonance generation more robust, expanding generation capabilities to encompass unstable resonances close to the secondary body, enable detecting resonance manifold intersections as an alternative to solving the TPBVP, and increasing the fidelity of the trajectories. Anderson, Vaquero, and Howell have developed intuition for resonance generation, selection, and manipulation. Capturing this intuition into autonomous algorithms would enable better initial guesses at solutions. Better initial guesses would enable DyLAN to converge to a family of solutions with fewer iterations. With fewer generations the overall runtime of the program would be reduced. Additionally, the GA internal parameters were held fixed for this work. It is possible these parameters could be tuned to better enable missions incorporating resonance orbits and their manifolds. Lastly, the missions could be expanded to include low-thrust propulsion and multiple phases. Each of these potential avenues are discussed in more detail in the following subsections.

7.2.1 Robust Manifold Generation vs Computational Efficiency

One of the major limitations of this work is the range of resonance orbits that can be generated robustly. The more resonance orbits that can be generated, the wider the design space and the more options the tool DyLAN has at its disposal for finding low energy transfers. This thesis incorporated multiple shooting and continuation schemes as a means of addressing this challenge; however, these two numeric techniques are not sufficient at producing a comprehensive range of resonance orbits. Additionally, these workarounds slow down the runtime of the tool and encumber the program with many checks and failsafes to prevent the likelihood of an orbit failing to generate.

To improve the computational efficiency of resonant orbit generation, robust continuation schemes should be developed and integrated. Pseudo-arc continuation does not continue along a physical dimension but rather along the solution function [42] where each point on the curve is a member of the resonance family. However, because the continuation is along the solution function, it is difficult to predict the continued states and thus difficult to target a specific resonance orbit.

Pseudo-arc continuation was explored briefly but abandoned due to time constraints. Further exploration in Pseudo-arc continuation as well as finer improvements in the continuation schemes implemented in this thesis could significantly increase the robustness and reduce computational complexity of resonance orbits.

An additional solution would be to read in values of pre-generated orbits stored in databases [52]. These databases can be extended to full families of orbits with the simple continuation schemes detailed in this thesis and would substantially reduce the computational complexity of generating a periodic orbit.

7.2.2 Resonance Orbits Close to the Secondary

Anderson utilized resonance orbits as a means of slowing down a spacecraft's approach towards Europa in the Jovian system [22]. The close approach distance on the secondary body during the designed resonance orbits were much closer than is traditionally used. Resonance orbits that approach the secondary body are difficult to generate because they stop following the two-body approximations detailed in section 4.1.1 and their period becomes less predictable because the spacecraft tends to linger by the secondary body. Anderson details some techniques for generating resonance orbits close to the secondary but acknowledges that there is still future work to be done in this area [43]. These techniques were beyond the scope of this initial work in automating resonance orbits, but are a strong avenue for future development. This feature would enable DyLAN to solve an expanded set of mission profiles such as consecutive secondary flybys as a means of being captured in an orbit about the secondary.

7.2.3 Manifold Intersections

Vaquero and Anderson have both shown Poincare sections to display the intersection of resonance manifold arcs [25] [38]. The benefit of looking at these surfaces is that it guarantees the two arcs are matching in position and in one of the two velocity components. Usually, only a minor Δv is required to transition from one arc to another. Intersection on a Poincare section eliminates the need for solving a TPBVP between arcs altogether and results in a very fuel-efficient transport (sometimes at the cost of TOF). Detecting these shapes and more importantly where two shapes intersect autonomously is a significant amount of effort.

7.2.4 High Fidelity Modeling

DyLAN has been developed to be a preliminary mission design tool. This means results from DyLAN would enable mission level decisions at an early point in the process. DyLAN currently works in the CR3BP because it is a significant increase in fidelity from a two-body or even patched conic model. However, as detailed in section 2.3 the CR3BP has major underlying assumptions that are not truly present in the physical universe. Increasing the fidelity of the models used would increase the correlation between design and reality. Therefore, adding more fidelity to DyLAN would strengthen its utility for preliminary mission design. Increasing fidelity can be achieved via two strategies. One strategy would be to upgrade the models used. Upgrading the models means transitioning from the CR3BP equations of motion to the four-body problem or higher dimensions of problems. Additionally, the bodies would be orbiting in their true motions such as in the elliptical three-body problem. Furthermore, spherical harmonics could be used instead of the point mass assumptions to better model the gravitational effects on the spacecraft. The second strategy would be to use the trajectory produced in the lower fidelity three-body model as an initial guess for a solver in an n-body environment such as GMAT. Both strategies require a substantial amount of effort but either would greatly increase the confidence in solutions produced by DyLAN when making critical mission level design decisions.

7.2.5 Outer Loop Tuning

The genetic algorithm has several internal parameters that influence the evolution of individuals over the generations. There are a number of parameters such as mutation rate, cross over rate, elitism percent, as well as the population size and number of generations. The work in this thesis held these values constant for all three missions. It is a worthwhile effort to study how these parameters affect the convergence of solutions and if different combinations of parameters converge to different solution spaces entirely.

7.2.6 Low-Thrust Propulsion

This work uses impulsive thrust as the only means for a spacecraft performing a burn to change its velocity. However, modern missions are diverging from impulsive thrust and beginning to use

low-thrust, such as electric propulsion, more regularly. Studying resonance transfers with low-thrust would build off observations made by Anderson [21] [24] [38] and expand the mission capabilities for DyLAN. There are a number of low-thrust transcriptions that would need to be seriously considered such as temporal distribution vs spatial distribution [53] of control nodes and how to manage the large volume of decision variables in DyLAN's hybrid optimal control algorithm.

7.2.7 Multi-phase Transfers

Using resonance orbits as an intermediate orbit for a mission or linking multiple resonance orbits together is a logical progression from the single-phase trajectory work presented here. Historically, Lyapunov orbits and their manifolds have been sought after as means for LEO to low lunar orbit. Using resonance dynamical structure instead of Lyapunov orbits and their manifolds is an interesting challenge that would be of significant value to the astrodynamicist community. With multi-phase mission design the trajectories can be a unique combination of resonance orbits and Lyapunov orbits to accomplish a desired mission. Vaquero showed a LEO to resonance to Lyapunov orbit about the L4 equilibrium point [42]. Building off her techniques and incorporating them into an automated algorithm for multi-phase mission analysis is an important follow on to the work in presented in this thesis.

7.3 Conclusion

The work detailed in this thesis demonstrates resonance orbits and their invariant manifolds in an automated hybrid optimal control software package called DyLAN. Example missions such as LEO to cislunar space and resonance to resonance transfers are solved for and discussed at length. Future work on improving the capabilities of DyLAN and how the software can efficiently utilize the resonance dynamical structure are also discussed. The aforementioned future work will benefit the field of trajectory design in the three-body problem because DyLAN provides a platform for preliminary mission level trajectory design in a way that does not depend on a human in-the-loop. Moving towards automated solutions will enable rapid prototyping of missions and thus increase the likelihood that a prospective mission becomes realized.

REFERENCES

[1] D. J. Dichmann, J. J. K. Parker, T. W. Williams and C. R. Mendelsohn, "Trajectory Design For The Transiting Exoplanet Survey Satellite," NASA Goddard Space Flight Center, Greenbelt, MD, 2016.

[2] J. Carrico Jr. , D. Dichmann, L. Policastri, J. Carrico III, T. Craychee, J. Ferreira, M. Intelisano, R. Lebois, M. Loucks, T. Schrift and R. Sherman, "Lunar-Resonant Trajectory Design For The Interstellar Boundary Explorer (IBEX) Extended Mission," in *AIAA/AAS Spaceflight Mechanics Conference*, Williamsburg, VA, 2012.

[3] I. Newton, Philosophiae Naturalis Principia Mathematica, 1687.

[4] J.-L. Lagrange, Tome 6, Chapitre II: Essai sur le probleme des trois corps, Paris: Academie Royale Des Sciences de Paris, 1772.

[5] L. Euler, "De motu rectilineo trium corporum se mutuo attrahentium," *Novi Commentarii academiae scientiarum Petropolitanae,* vol. 11, pp. 144-151, 1767.

[6] H. G. Hill, "Researches in the Lunar Theory," *American Journal of Mathematics,* vol. 1, no. 1, pp. 5-26, 1878.

[7] H. Poincare, Les methodes nouvelles de la mechanique celeste, Paris: Gauthier-Villars, 1899.

[8] K. T. Alligood, T. Sauer and J. A. Yorke, Chaos: An Introduction to Dynamical Systems, New York: Springer-Verlag, 1996.

[9] C. C. Conley, "Low Energy Transit Orbits in the Restricted Three-Body Problem," *SIAM Journal of Applied Mathematics,* vol. 16, pp. 732-746, 1968.

[10] K. Howell and L. Hiday-Johnston, "Time-Free Transfers between Libration-Point Orbits in the Elliptic Restricted Problem," *Acta Astronautica,* vol. 32, no. 4, pp. 245-254, 1994.

[11] L. Hiday-Johnston and K. Howell, "Impulsive Time-Free Transfers between Halo Orbits," *Celestial Mechanics and Dynamical Astronomy,* vol. 44, no. 2, pp. 281-904, 1996.

[12] K. Howell, B. Barden and M. Lo, "Application of Dynamical Systems Theory to trajectory Design for a Libration Point Mission," *Journal of the Astronautical Sciences,* vol. 45, no. 2, pp. 161-178, 1997.

[13] M. Lo, B. Williams, W. Bollman, D. Han, Y. Hahn, J. Bell, E. Hirst, R. Corwin, P. Hong, K. Howell, B. Barden and R. Wilson, "GENESIS Mission Design," *Journal of the Astronautical Sciences,* vol. 49, no. 1, pp. 169-184, 2001.

[14] W. S. Koon, M. W. Lo, J. E. Marsden and S. D. Ross, Dynamical Systems, the Three-Body Problem and Space Mission Design, Passadena, CA, 2006.

[15] J. S. Parker and R. L. Anderson, Low-Energy Lunar Trajectory Design, Volume 12 of JPL Deep Space Communications and Navigation Series, 1st edn., Hoboken, NJ: Wiley, 2014.

[16] V. Domingo, B. Fleck and A. I. Poland, "The SOHO Mission: An Overview," Kluwer Academic Publishers, Belgium, 1995.

[17] E. C. Stone, A. M. Frandsen, R. A. Mewaldt, E. R. Christian, D. Margolies, J. F. Ormes and F. Snow, "The Advanced Composition Explorer," *Space Science Reviews,* vol. 86, no. 1-4, pp. 1-22, 1998.

[18] J. P. Gardner, J. C. Mather, M. Clampin, R. Doyon, M. A. Greenhouse, H. B. Hammel, J. B. Hutchings, P. Jakobsen, S. J. Lilly, K. S. Long, J. I. Lunine, M. J. McCaughrean, M. Mountain, J. Nella, G. H. Rieke, M. J. Rieke, H.-W. Rix, E. P. Smith, G. Sonneborn, M. Stiavelli, H. S. Stockman, R. A. Windhorst and G. S. Wright, "The James Webb Space Telescope," Space Science Reviews, 2006.

[19] C. G. Schroer and E. Ott, "Targeting in Hamiltonian systems that have mixed regular/chaotic phase spaces," *Chaos 7*, pp. 512-519, 1997.

[20] R. L. Anderson and M. W. Lo, "A dynamical systems analysis of planetary flybys and approach: ballistic case," *Journal of Astronautical Sciences,* vol. 58, no. 2, pp. 167-194, 2011.

[21] R. L. Anderson and M. W. Lo, "Role of Invariant Manifolds in Low-Thrust Trajectory Design (Part III)," *Journal of Guidance, Control, and Dynamics,* vol. 32, no. 6, pp. 1921-1930, 2009.

[22] R. L. Anderson and M. W. Lo, "A dynamical systems analysis of planetary flybys and approach: planar Europa Orbiter," *Journal of Guidance Control and Dynamics,* vol. 22, no. 6, pp. 1899-1912, 2010.

[23] M. W. Lo, R. L. Anderson, G. Whiffen and L. Romans, "The Role of Invariant Manifolds in Low Thrust Trajectory Design (Part I)," in *AAS/AIAA Spaceflight Dynamics Conference*, Maui, Hawaii, 2004.

[24] R. L. Anderson and M. W. Lo, "The Role of Invariant Manifolds in Low Thrust Trajectory Design (Part II)," in *AIAA/AAS Spaceflight Mechanics Conference*, Copper Mountain, Colorado, 2004.

[25] T. M. Vaquero Escribano, "Poincare Sections and Resonant Orbits in the Restricted Three-Body Problem," Purdue University, West Lafayette, IN, 2010.

[26] M. Vaquero and K. C. Howell, "Design of Transfer Trajectories Between Resonant Orbits in the Restricted Problem with Application to the Earth-Moon System," in *1st IAA Conference on Dynamics and Control of Space Systems*, Porto, Portugal, 2012.

[27] M. Vaquero and K. C. Howell, "Leveraging Resonant Orbit Manifolds to Design Transfers Between Libration Point Orbits in Multi-Body Regimes," in *AIAA/AAS Space Flight Mechanics Meeting*, Kauai, Hawaii, 2013.

[28] G. Lantoine, R. P. Russell and S. Campagnola, "Optimization of low-energy resonant hopping transfers between planetary moons," *Acta Astronautica,* vol. 68, no. 7, pp. 1361-1378, 2011.

[29] J. Englander, D. Ellison and M. Vavrina, *EMTG: Evolutionary Mission Trajectory Generator v.8,* https://opensource.gsfc.nasa.gov/projects/emtg/index.php, 2017.

[30] J. A. Englander and B. A. Conway, "Automated Solution of the Low-Thrust Interplanetary Trajectory Problem," *Journal of Guidance, Control, and Dynamics,* vol. 40, pp. 15-27, 2017.

[31] G. Rauwolf and V. Coverstone-Carroll, "Low-Thrust Orbit Transfers Generated by a Genetic Algorithm," *Journal of Spacecraft and Rockets,* vol. 33, pp. 859-862, 1996.

[32] V. Coverstone-Carroll, J. Hartmann and W. Mason, "Optimal Multi-Objective Low-Thrust Spacecraft Trajectories," *Computer Methods in Applied Mechanics and Engineering,* vol. 186, pp. 387-402, 2000.

[33] V. Coverstone-Carroll, "Near-Optimal Low-Thrust Trajectories via Micro-Genetic Algorithms," *Journal of Guidance, Control, and Dynamics,* vol. 20, no. 1, pp. 196-198, 1997.

[34] J. Hartmann, V. Coverstone-Carroll and S. Williams, "Optimal Spacecraft Interplanetary Trajectories via a Pareto Genetic Algorithm," *Journal of the Astronautical Sciences,* vol. 46, no. 3, pp. 267-282, 1998.

[35] V. Shah, R. Beeson and V. Coverstone, "Automated Global Optimization of Multi-Phase Trajectories in the Three-Body Problem Using a Variable Gene Transcription," in *AIAA/AAS Space Flight Mechanics Conference,* San Antonio, TX, 2017.

[36] J. Aurich, Automated Detection of Invariant Manifold Intersections Using Grid Based Approach, Urbana-Champaign: University of Illinois at Urbana-Champaign, 2017.

[37] J. Aurich, R. Beeson and V. Coverstone, "Automated Detection of Invariant Manifold Intersections Using Adaptive Grid Method," in *AIAA/AAS SPACE 2016 Conference,* Long Beach, CA, 2016.

[38] R. L. Anderson, Low Thrust Trajectory Design for resonant Flybys and Captures Using Invariant Manifolds, University of Boulder, Colorado: Dissertation, 2005.

[39] J. E. Prussing and B. A. Conway, Orbital Mechanics 2nd ed., Oxford, New York: Oxford University Press, 2013.

[40] C. Short, K. Howell, A. Haapala and D. Dichmann, "Mode Analysis for Long-Term Behavior in a Resonant Earth-Moon Trajectory," *Journal of the Astronautical Sciences,* 2016.

[41] W. H. Press, S. A. Teukolsky, W. T. Vetterling and B. P. Flannery, Numerical Recipes in C++: The Art of Scientific Computing, Cambridge, United Kingdom: Cambridge University Press, 2002.

[42] T. M. Vaquero Escribano, "Spacecraft Transfer Trajectory Design Exploiting Resonant Orbits in Multi-Body Environments," Purdue University, West Lafayette, IN, 2013.

[43] R. L. Anderson, S. Campagnola and G. Lantoine, "Broad search for unstable resonant orbits in the planar circular restricted three-body problem," *Celestrial Mechanics, Dynamics, and Astrophysics,* vol. 124, pp. 177-199, 2016.

[44] R. L. Anderson and M. W. Lo, "Dynamical Systems Analysis of Planetary Flybys and Approach: Planar Europa Orbiter," *Journal of Guidance, Control, and Dynamics,* vol. 33, no. 6, pp. 1899-1912, 2010.

[45] G. Floquent, "Sur les equations differentielles lineaires a coefficients periodiques," *Annales de L'Ecole Normale Superieure* , vol. 12, pp. 47-88, 1883.

[46] J. V. Breakwell, "The Optimization of Trajectories," *Journal of the Society for Industrial and Applied Mathematics,* vol. 7, no. 2, pp. 215-247, 1959.

[47] J. Englander and B. A. Conway, "Automated Solution of the Low-Thrust Interplanetary Trajectory Problem," *Journal of Guidance, Control, and Dynamics,* vol. 40, no. 1, pp. 15-27, 2016.

[48] V. Pareto, "Manuale di Economia Politica," Societa Editrice Libraria, Milano, Italy, 1906.

[49] J. A. Englander, B. A. Conway and T. Williams, "Automated Mission Planning via Evolutionary Algorithms," *Journal of Guidance, Control, and Dynamics,* vol. 35, no. 6, pp. 1878-1887, 2012.

[50] V. Shah, "Automated Global Optimization of Low-Energy Trajectories Using a Hybrid Optimal Control Framework," University of Illinois , Urbana-Champaign, 2017.

[51] P. E. Gill, W. Murray and M. A. Saunders, "SNOPT: An SQP Algorithm for Large-Scale Contrained Optimization," *SIAM Review,* vol. 47, pp. 99-131, 2005.

[52] R. L. Restrepo and R. P. Russell, "A Database of Planar Axi-Symmetric Periodic Orbits for the Solar System," in *AAS/AIAA Astrodynamics Specialist Conference*, Stevenson, WA, August 2017.

[53] D. H. Ellison, J. A. Englander and B. A. Conway, "A Time-Regularized, Multiple Gravity-Assist Low-Thrust, Bounded-Impulse Model For Trajectory Optimization," in *AAS/AIAA Spaceflight Mechanics Conference*, San Antonio, TX, 2017.

[54] "GMAT User Guide R2016a," NASA Goddard, Greenbelt, MD, 2016.